Electronic Supplementary Information

Strain-based chemical detection using metal-organic framework nanoparticles

H. H.-M. Yeung,[a,b‡*] G. Yoshikawa,[c,d] K. Minami[b,c] and K. Shiba[b,c,e*]

a) School of Chemistry, University of Birmingham, Edgbaston, Birmingham, UK.
b) International Center for Young Scientists (ICYS), National Institute for Materials Science (NIMS), Tsukuba, Japan.
c) Center for Functional Sensor & Actuator (CFSN), Research Center for Functional Materials, National Institute for Materials Science (NIMS), Tsukuba, Japan.
d) Materials Science and Engineering, Graduate School of Pure and Applied Science, University of Tsukuba, Tsukuba, Japan
e) John A. Paulson School of Engineering and Applied Sciences, Harvard University, Cambridge, Massachusetts, United States.
‡ Previous address: Inorganic Chemistry Laboratory, University of Oxford, South Parks Road, Oxford, UK.
*Email: h.yeung@bham.ac.uk; SHIBA.Kota@nims.go.jp

Contents

S1. Synthesis

ZIF-7 nanoparticles. Nanoparticles of ZIF-7, $Zn(bIm)_2$ in **sod** topology, were synthesized by adapting the method of Li *et al*.[1] In detail, zinc nitrate hexahydrate (302 mg, 1 mmol) was dissolved in *N,N*-dimethylformamide (10 mL) and poured rapidly into a solution of benzimidazole (769 mg, 6.4 mmol) in *N,N*-dimethylformamide (10 mL) under stirring at room temperature. Stirring continued for 12 hours after which the milky suspension was centrifuged at 15000 g for 30 minutes. The supernatant was decanted and replaced by methanol and the mixture sonicated for one minute to redisperse the particulate matter. The centrifuge / washing process was repeated thrice more. Half the resulting suspension was kept for further use, and half was dried (60 °C in air, then 180 °C under active vacuum overnight), yielding an off-white solid, 104 mg (71 % yield based on Zn).

ZIF-8 nanoparticles. Nanoparticles of ZIF-8, $Zn(mIm)_2$ in **sod** topology, were synthesized by adapting the method of Cravillon *et al*.[2] In detail, zinc nitrate hexahydrate (297 mg, 1 mmol) was dissolved in methanol (20 mL) and poured rapidly into a solution of 2-methylimidazole (649 mg, 7.9 mmol) in methanol (20 mL) under stirring at room temperature. Stirring continued for 6.5 hours, after which the milky suspension was centrifuged at 15000 g for one hour. The supernatant was decanted and replaced by fresh methanol and the mixture sonicated for 5 minutes to redisperse the particulate matter. The centrifuge / washing process was repeated twice more. Half the resulting suspension was kept for further use, and half was dried (90 °C in air, then 180 °C under active vacuum overnight), yielding a pale yellow solid, 38 mg (35 % yield based on Zn).

ZIF-65-Zn nanoparticles. Nanoparticles of ZIF-65-Zn, $Zn(nIm)_2$ in **sod** topology, were synthesized by adapting the method of Tu *et al*.[3] In detail, zinc acetate dihydrate (110 mg, 0.5 mmol) was dissolved in *N,N*-dimethylformamide (5 mL) and poured rapidly into a solution of 2-nitroimidazole (113 mg, 1.0 mmol) in N,N-dimethylformamide (5 mL) under stirring at room temperature. Stirring continued overnight, after which the yellow milky suspension was centrifuged at 15000 g for 30 minutes. The supernatant was decanted and replaced by *N,N*-dimethylformamide and the mixture sonicated for one minute to redisperse the particulate matter. The centrifuge / washing process was repeated thrice more, using methanol as the fresh solvent. For the final centrifugation, the suspension was split into two equal fractions. One half was dried under vacuum at 55 °C overnight, yielding a yellow solid, 22.3 mg (39 % based on Zn). The other half was redispersed in IPA for sensing experiments.

ZIF-71 nanoparticles. Nanoparticles of ZIF-71, $Zn(dcIm)_2$ in **rho** topology, were synthesized by adapting the method of Tu *et al*.[3] In detail, zinc acetate dihydrate (220 mg, 1 mmol) was dissolved in *N,N*-dimethylformamide (10 mL) and poured rapidly into a solution of 4,5-dichloroimidazole (960 mg, 6 mmol) in *N,N*-dimethylformamide (10 mL) under stirring at room temperature. Stirring continued for four hours after which the milky suspension was centrifuged at 15000 g for 30 minutes. The supernatant was decanted and replaced by methanol and the mixture sonicated for one minute to redisperse the particulate matter. The centrifuge / washing process was repeated thrice more. Three quarters of the resulting suspension was kept for further use, and one

quarter was dried (60 °C in air, then 180 °C under active vacuum overnight), yielding a brown powder, 75 mg (92 % yield based on Zn).

S2. Powder X-ray diffraction
Samples were analysed on Rigaku Ultima3 or RINT2000 instruments in a θ-2θ flat plate geometry using Cu K-α radiation. Data were collected from 2 ° to 50 ° 2θ.

ZIF-7 nanoparticles (Fig. S1) exhibited reasonable crystallinity when as-synthesized and washed, with peak positions consistent with the theoretical pattern simulated using data from Zhao *et al*.[4] Upon heating at 180 °C under vacuum—conditions that are much harsher than those used for device fabrication—crystallinity was largely lost, as evident from the reduction of definition and intensity of the diffraction peaks.

ZIF-8 nanoparticles (Fig. S2) exhibited a good match to the pattern simulated using data from Park *et al*.[5] and very little difference between XRD patterns as-synthesized and washed and dried. The crystal structure was maintained even when activated at 180 °C under vacuum.

ZIF-65-Zn nanoparticles (Fig. S3) also exhibited a close match to the pattern simulated using data from Banerjee *et al*.[6] Very little difference was observed between the patterns of as-synthesized, washed and dried, and activated material.

ZIF-71 nanoparticles (Fig. S4) exhibited lower crystallinity when as-synthesized than the other materials investigated, although the positions of the XRD peaks match the pattern simulated using data from Banerjee *et al*.[6] well. A similar degree of crystallinity is retained after washing and drying, and after activation.

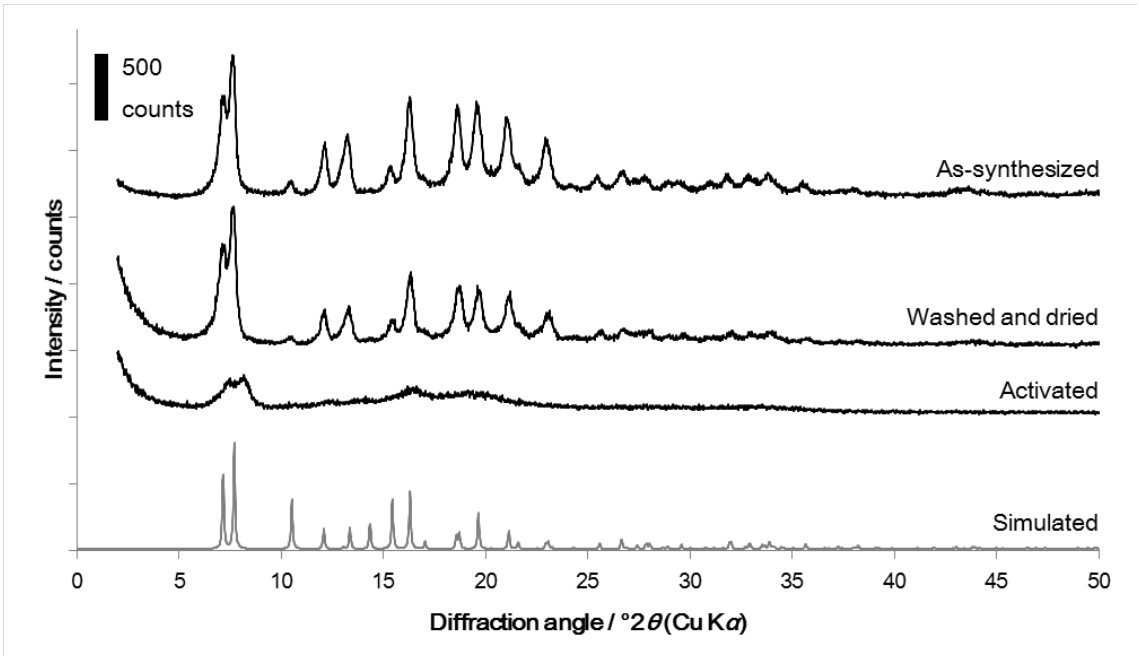

Fig. S1. XRD patterns of ZIF-7 nanoparticles: as-synthesized, washed and dried in vacuo at room temperature, and activated at 180 °C in vacuo. The theoretical, simulated pattern is shown below for comparison.

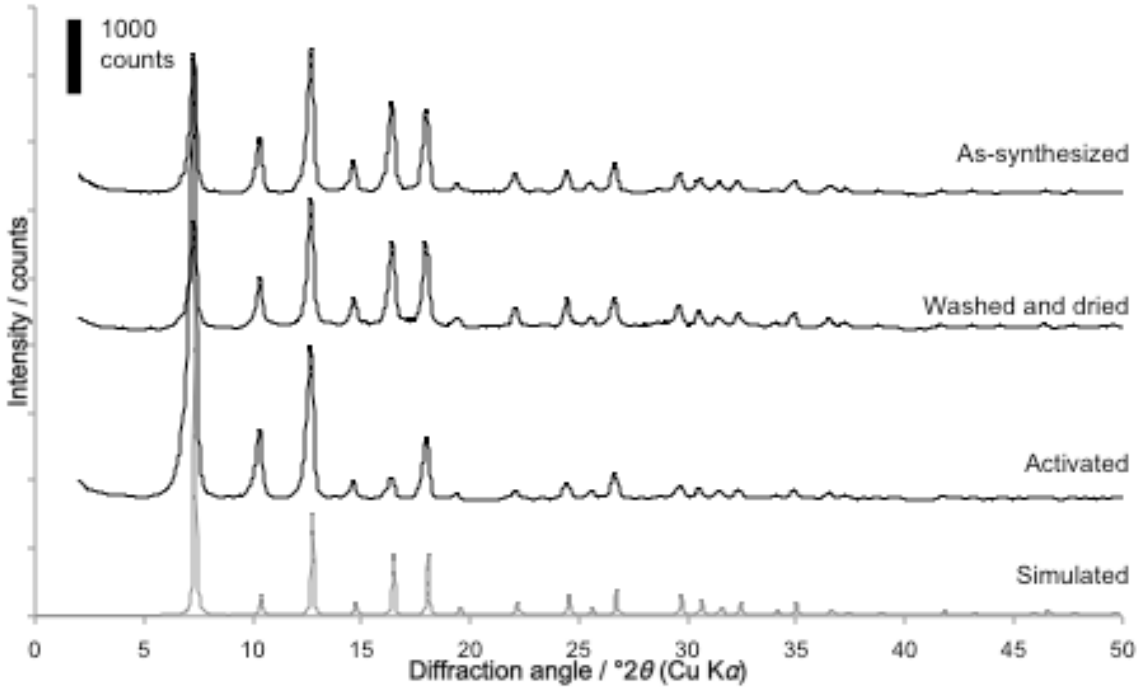

Fig. S2. XRD patterns of ZIF-8 nanoparticles: as-synthesized, washed and dried in vacuo at room temperature, and activated at 180 °C in vacuo. The theoretical, simulated pattern is shown below for comparison.

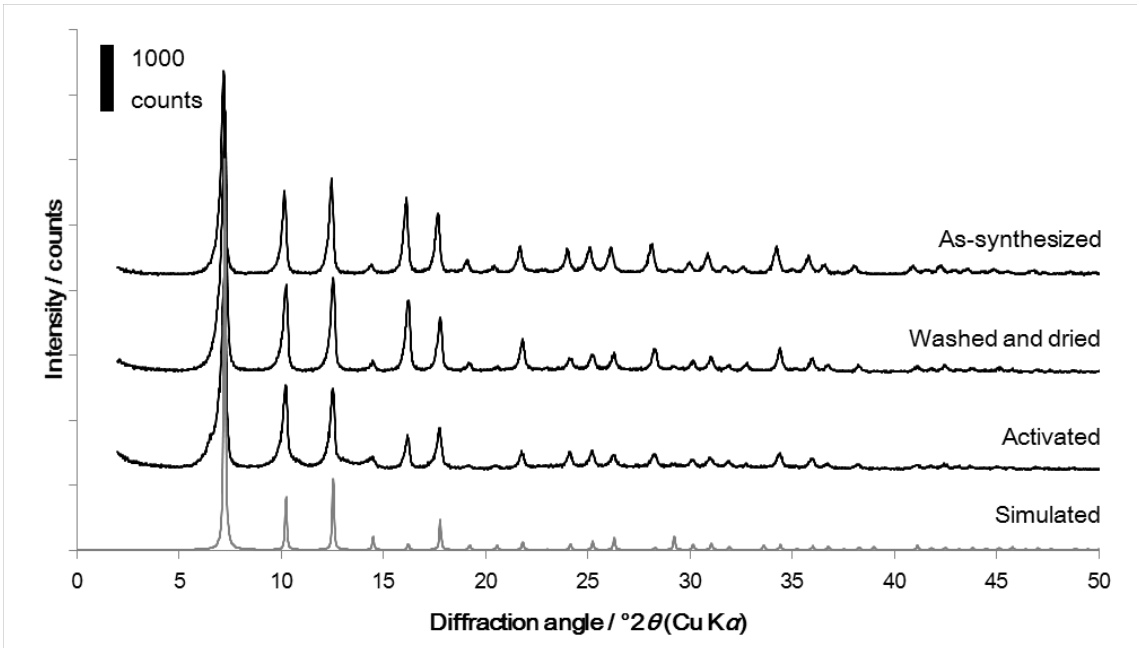

Fig. S3. XRD patterns of ZIF-65-Zn nanoparticles: as-synthesized, washed and dried in vacuo at room temperature, and activated at 180 °C in vacuo. The theoretical, simulated pattern is shown below for comparison.

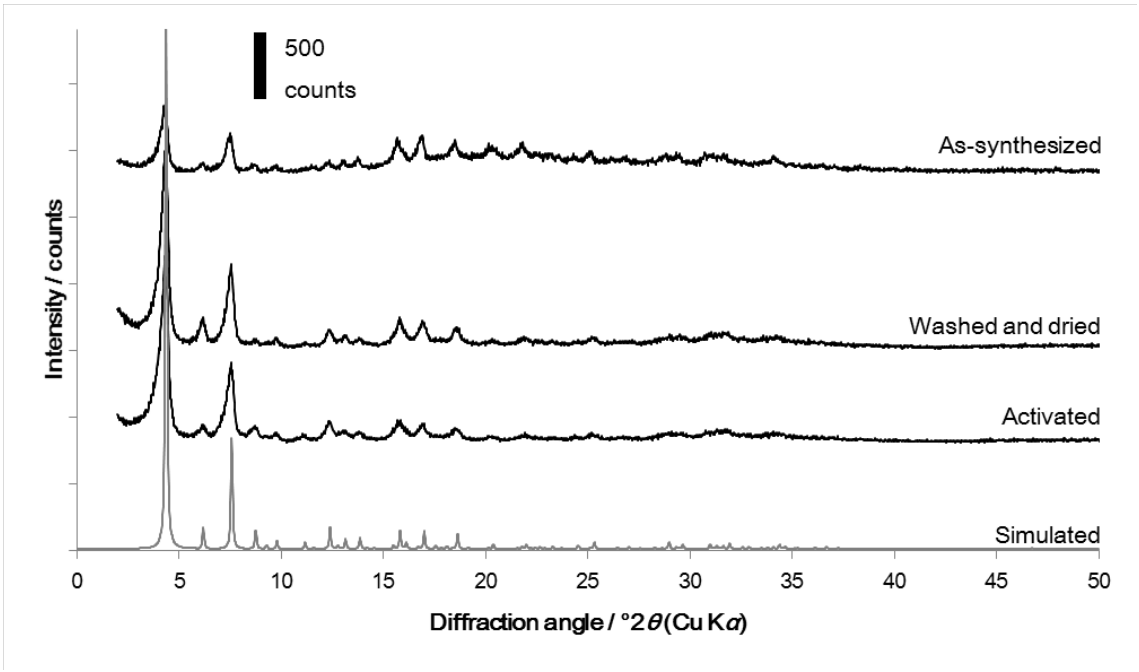

Fig. S4. XRD patterns of ZIF-71 nanoparticles: as-synthesized, washed and dried in vacuo at room temperature, and activated at 180 °C in vacuo. The theoretical, simulated pattern is shown below for comparison.

S3. Infrared spectra

Fourier transform infrared (FTIR) spectra were recorded on a Thermo Nicolet spectrometer with ATR attachment, under a flow of nitrogen, for each material after washing and drying under vacuum at room temperature, and after activation at 180 °C under vacuum. In the spectra of samples that have been washed and dried at room temperature, broad peaks in the region 2700–3500 cm^{-1} (O-H stretching, methanol), strong peaks at around 1700 cm^{-1} (C=O stretching, DMF) and 2800–3000 cm^{-1} (CH_3 stretching, methanol/DMF) are suggestive of solvent that remains in the pores after washing. The peak at around 1400 cm^{-1} in the spectrum of ZIF-71 corresponds to precursor acetate ions (antisymmetric stretch). All these peaks are not present in the activated sample spectra, indicating that the solvents have been removed.

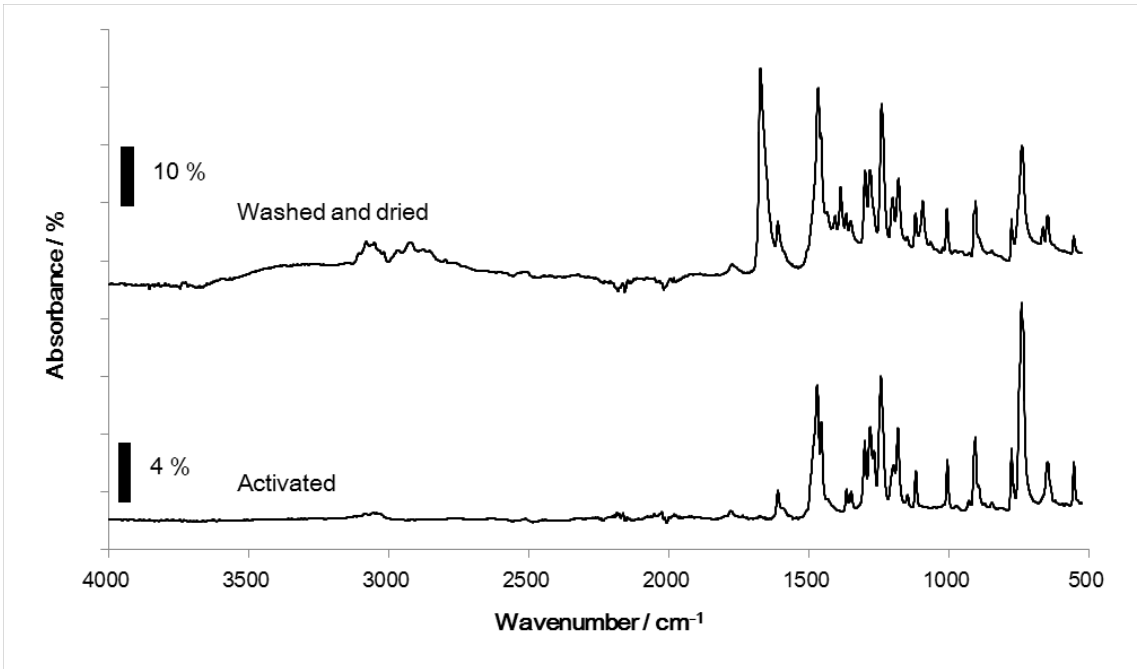

Fig. S5. Infrared spectrum of ZIF-7 nanoparticles, after washing and drying in vacuo at room temperature, and after activation in vacuo at 180 °C.

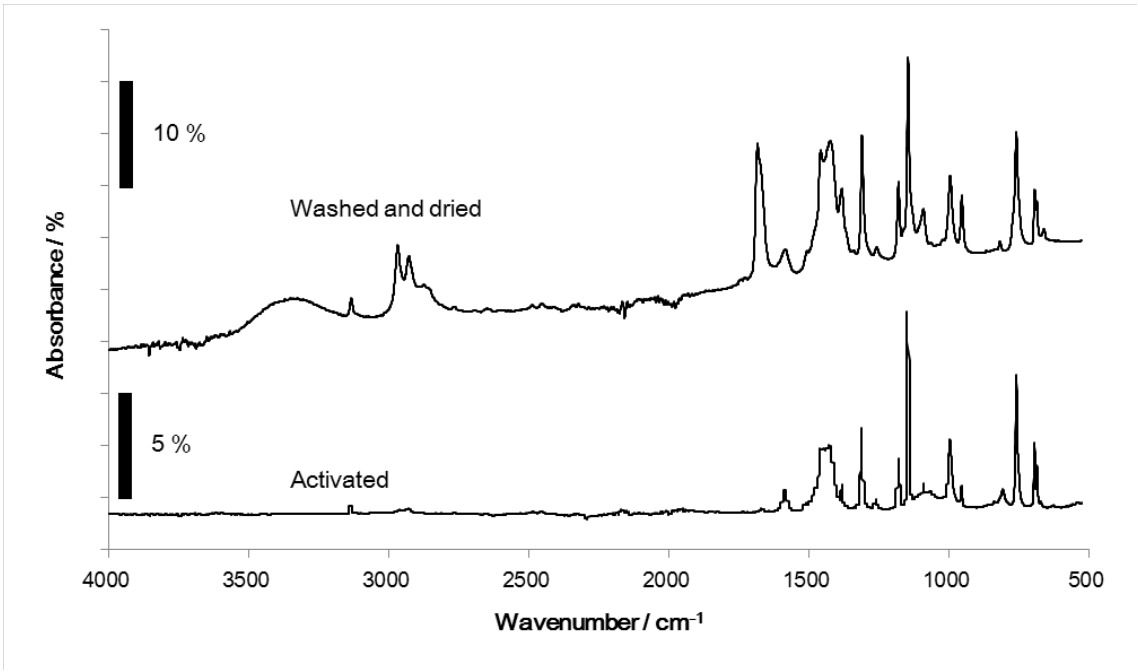

Fig. S6. Infrared spectrum of ZIF-8 nanoparticles, after washing and drying in vacuo at room temperature, and after activation in vacuo at 180 °C.

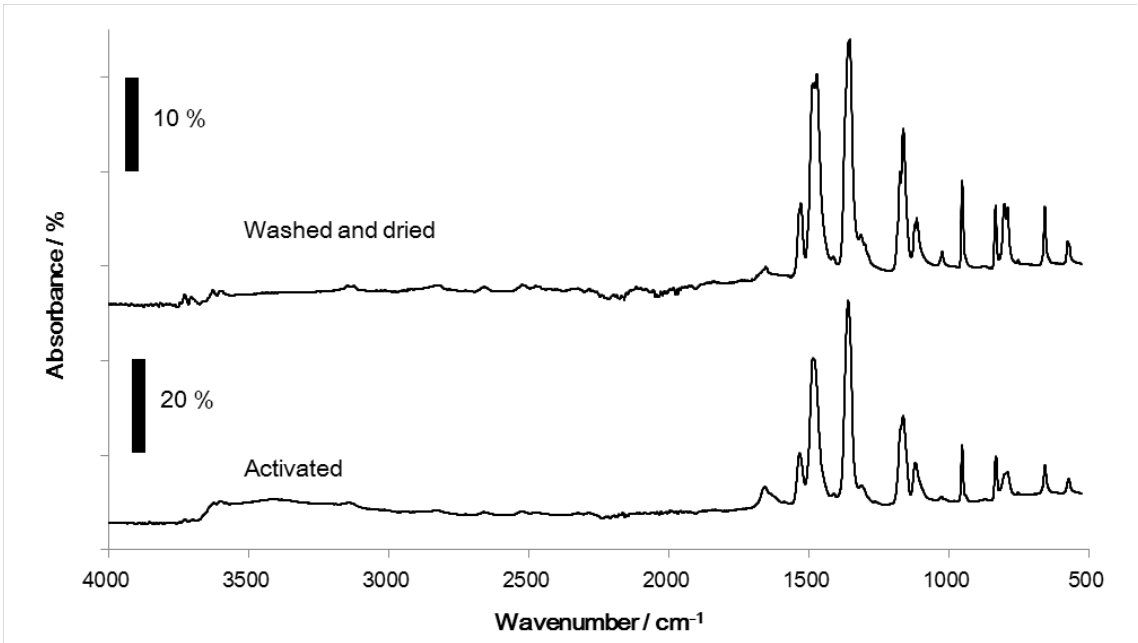

Fig. S7. Infrared spectrum of ZIF-65-Zn nanoparticles, after washing and drying in vacuo at room temperature, and after activation in vacuo at 180 °C.

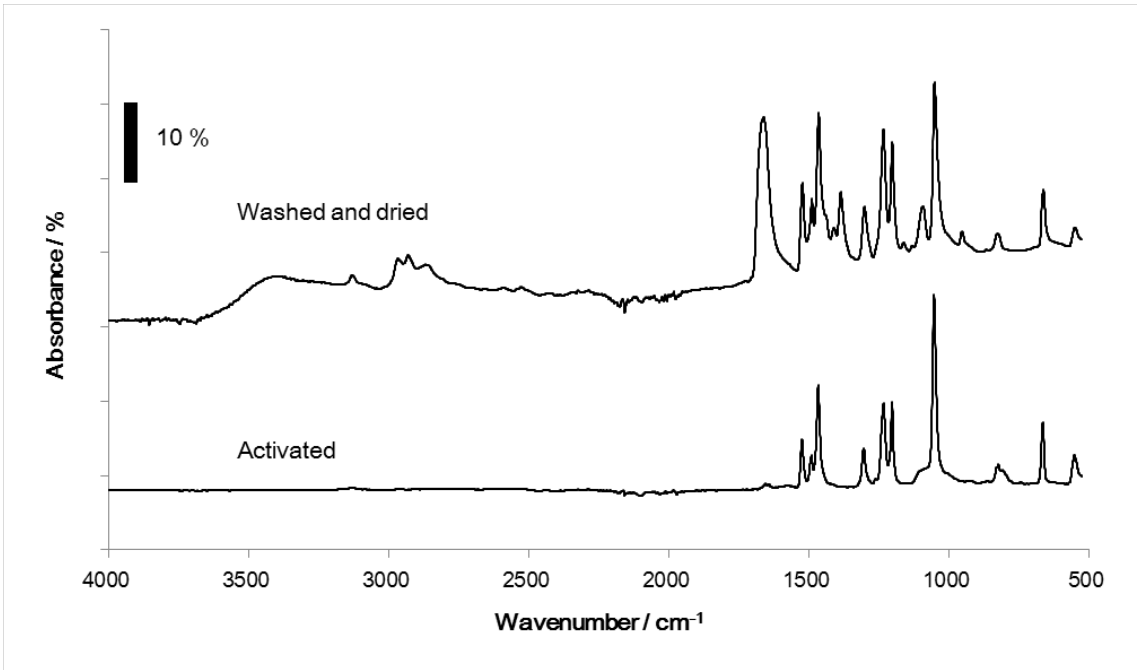

Fig. S8. Infrared spectrum of ZIF-71 nanoparticles, after washing and drying in vacuo at room temperature, and after activation in vacuo at 180 °C.

S4. Scanning electron microscopy

Scanning electron microscopy (SEM) images were acquired at magnifications between 20,000× and 200,000×, using a Hitachi SU8000 FE-SEM in backscattered electron imaging mode. Working distances between 4.6 and 8.0 mm were used, with 2.5 kV and 1.5 kV acceleration and deceleration voltages, respectively. The images show that each sample consists of agglomerated particles with sizes ranging from 50 nm to 200 nm; the most monodisperse were ZIF-8 particles, which had the most well-defined rhombic dodecahedral morphology.

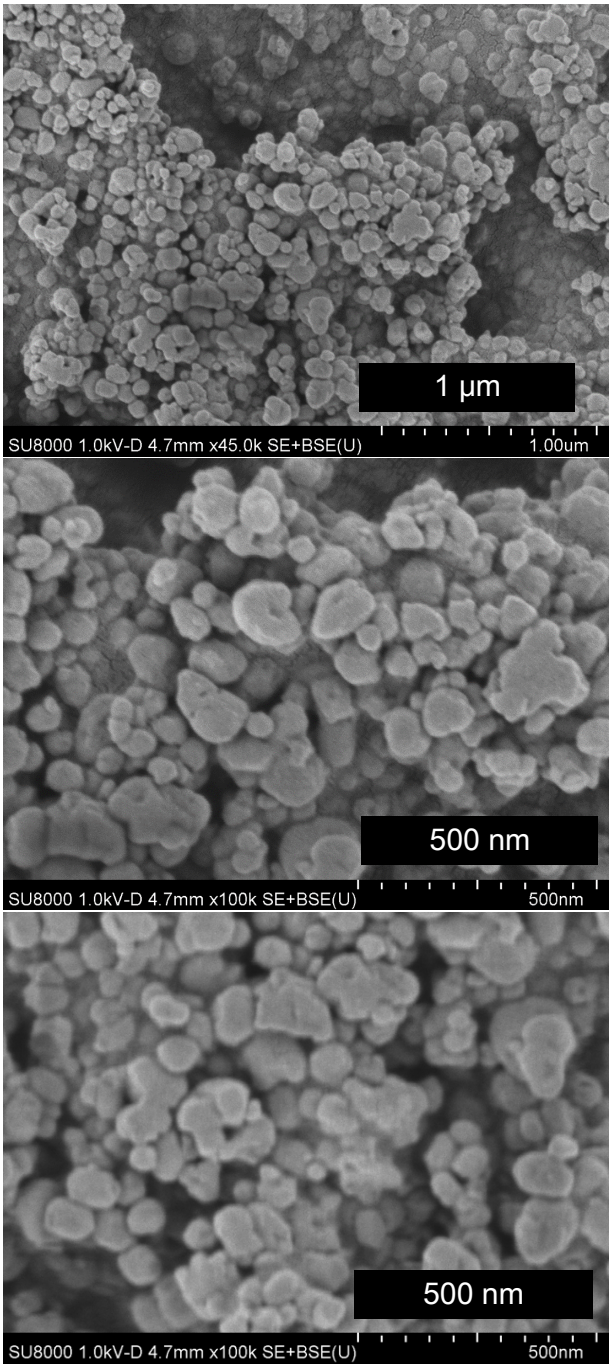

Fig. S9. SEM images of ZIF-7 nanoparticles.

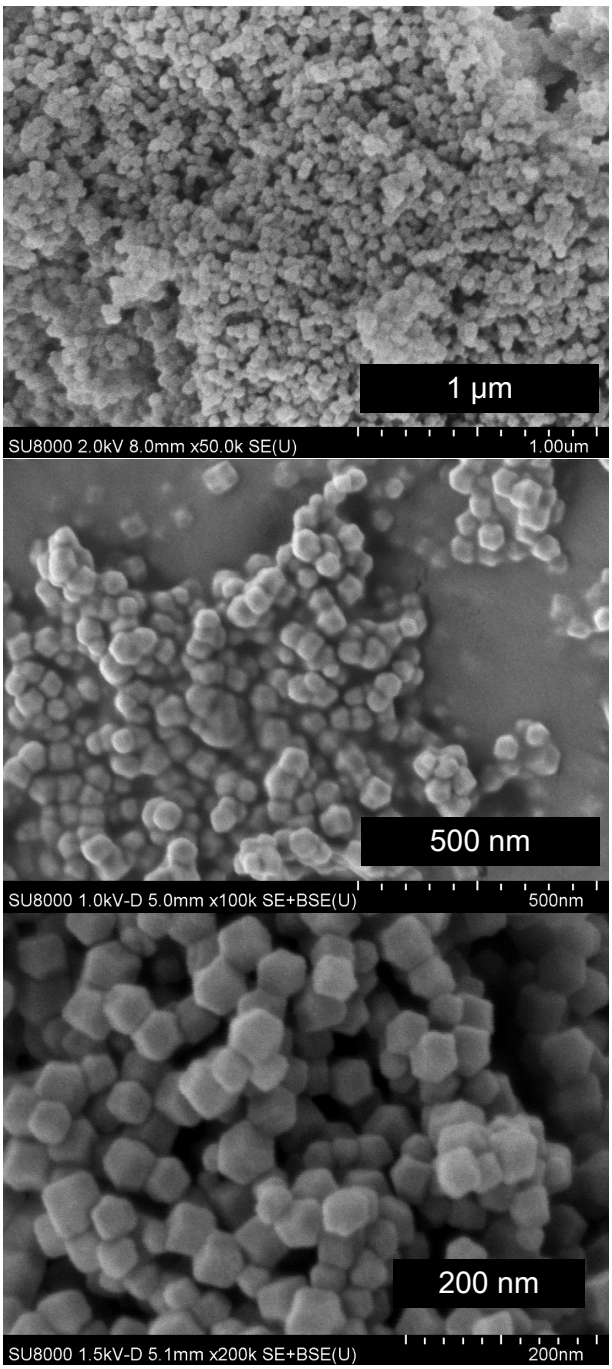

Fig. S10. SEM images of ZIF-8 nanoparticles.

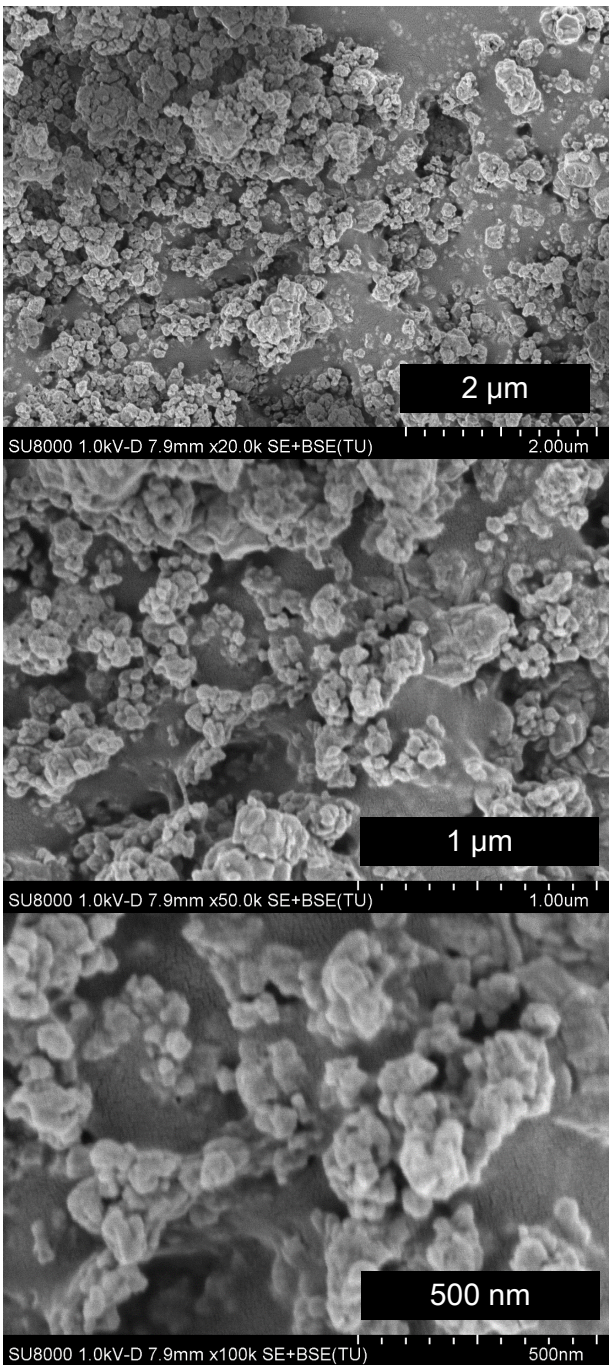

Fig. S11. SEM images of ZIF-65-Zn nanoparticles.

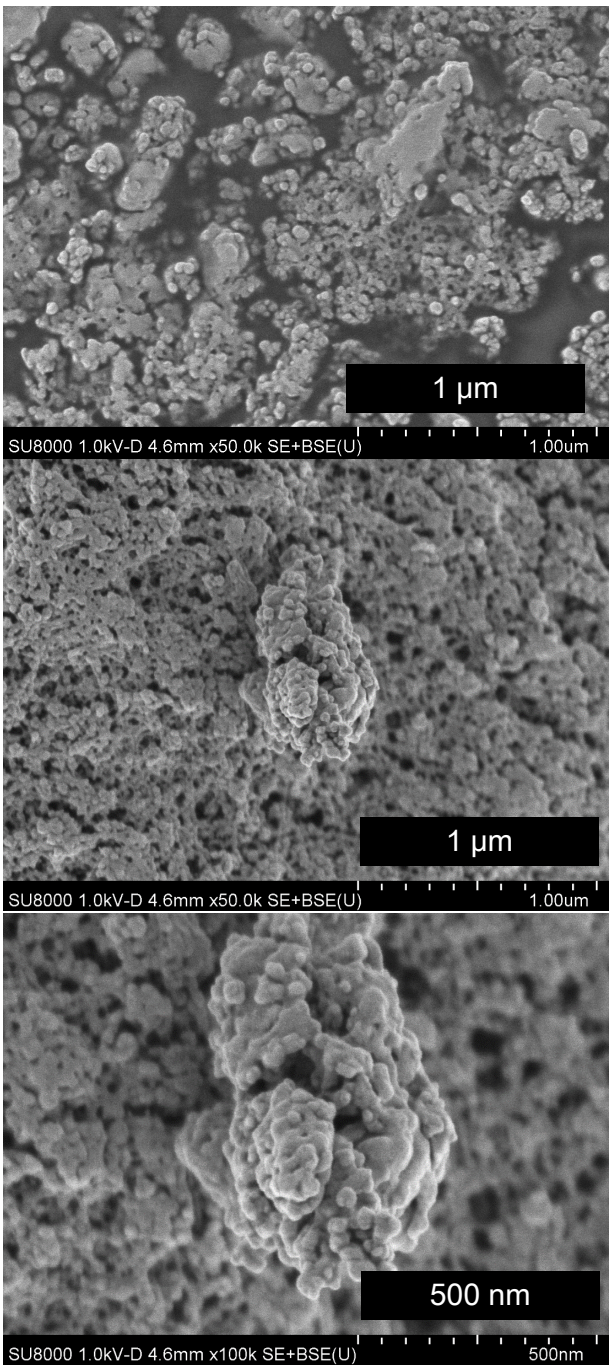

Fig. S12. SEM images of ZIF-71 nanoparticles.

S5. Dynamic light scattering and zeta potential

Dynamic light scattering (DLS) and zeta potential measurements were performed on diluted nanoparticle suspensions using an Otsuka Electronics ELSZ-2000 instrument. Comparing the SEM results to the particle diameters obtained in this way suggests that, after washing, the suspended particles are made up of several agglomerated smaller particles.

Table S1. Dynamic light scattering data for the ZIF nanoparticle suspensions.

	Suspension medium	Mean particle diameter / nm	Polydispersity index	Zeta potential / mV	Mobility / cm^2/Vs
ZIF-7	IPA	90	0.153	46	3.443×10^{-5}
ZIF-8	Methanol	186	0.102	31.2	1.695×10^{-4}
ZIF-65-Zn	IPA	374	0.216	307	2.292×10^{-4}
ZIF-71	IPA	196	0.239	–55	-4.1×10^{-5}

S6. Nitrogen sorption

Nitrogen sorption isotherms were collected at 77 K on samples activated at 180 °C for 48 hours in the pressure range $10^{-6} < P/P_0 < 1$, using a Quantachrome Autosorb iQ instrument. Surface areas were calculated from Brunauer-Emmett-Teller (BET) theory using data in the region $0.05 < P/P_0 < 0.3$. The data (Figs. S13–15) are broadly consistent with existing literature; notably evidence for the two-step isotherm can be seen for ZIF-8, and ZIF-7 exhibits very little adsorption owing to structure collapse upon activation.

Table S2. BET surface areas for ZIF nanoparticles.

	BET surface area / m^2/g
ZIF-7	224.3
ZIF-8	1269.7
ZIF-65-Zn	642.4
ZIF-71	803.3

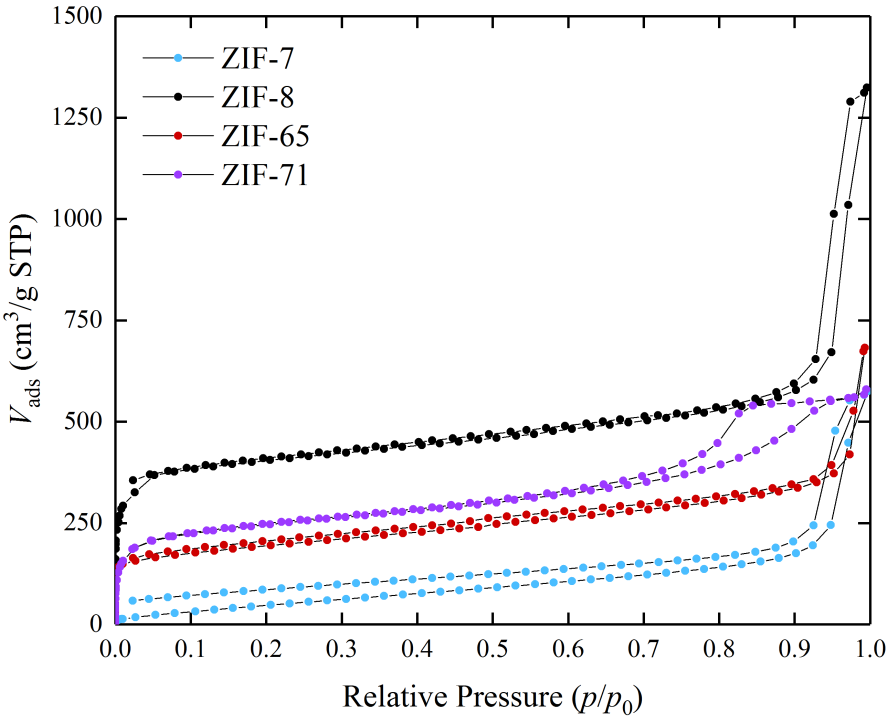

Fig. S13. Nitrogen sorption isotherms for ZIF nanoparticles, showing the full pressure range.

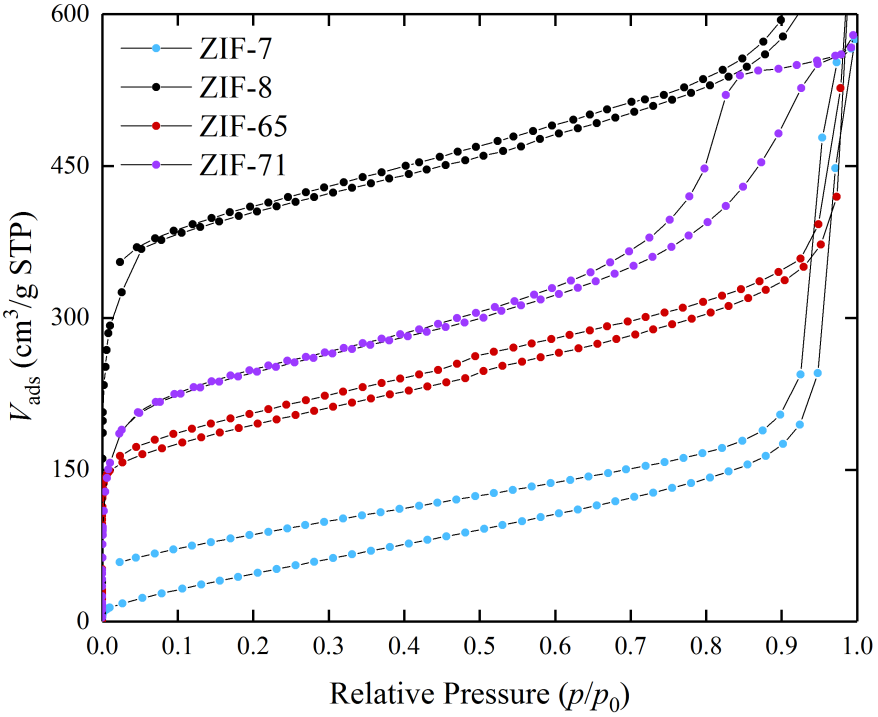

Fig. S14. Nitrogen sorption isotherms for ZIF nanoparticles, showing the *meso*- and microporous adsorption regime enlarged.

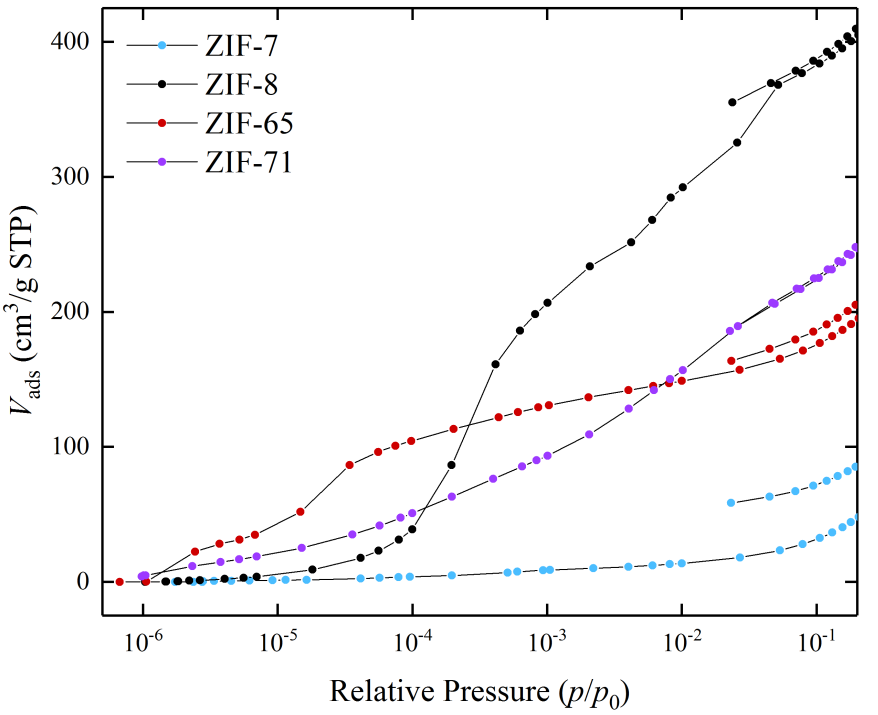

Fig. S15. Nitrogen sorption isotherms for ZIF nanoparticles, showing the low pressure region using a semi-log scale.

S7. Thermogravimetry

Thermogravimetric analysis was performed using a Perkin Elmer Diamond combined TG/DTA instrument. Activated samples were heated at a heating rate of 10 °C/minute under a constant air flow and differential thermal analysis was simultaneously conducted with reference to Al_2O_3 powder. Mass change data are plotted below as a function of time (a) and temperature (b) for each of ZIF-7, ZIF-8, ZIF-65-Zn and ZIF-71, for which the starting masses were 7.21 mg, 6.86 mg, 6.53 mg and 7.11 mg, respectively. Final masses were 1.97 mg for ZIF-7 (corresponding to ZnO, calculated 2.01 mg), 2.32 mg for ZIF-8 (corresponding to ZnO, calculated 2.55 mg), –0.09 mg for ZIF-65-Zn (corresponding to full evaporation) and 0.34 mg for ZIF-71 (corresponding to near-complete evaporation).

Where the mass change vs. temperature data turn back on themselves, we attribute this to the strongly exothermic decomposition process observed in the DTA signal for each material and the subsequent need for cooling the samples to return to the programmed temperature ramp profile. The actual temperature and deviation from programmed temperature data are plotted as a function of time in (c) for each ZIF.

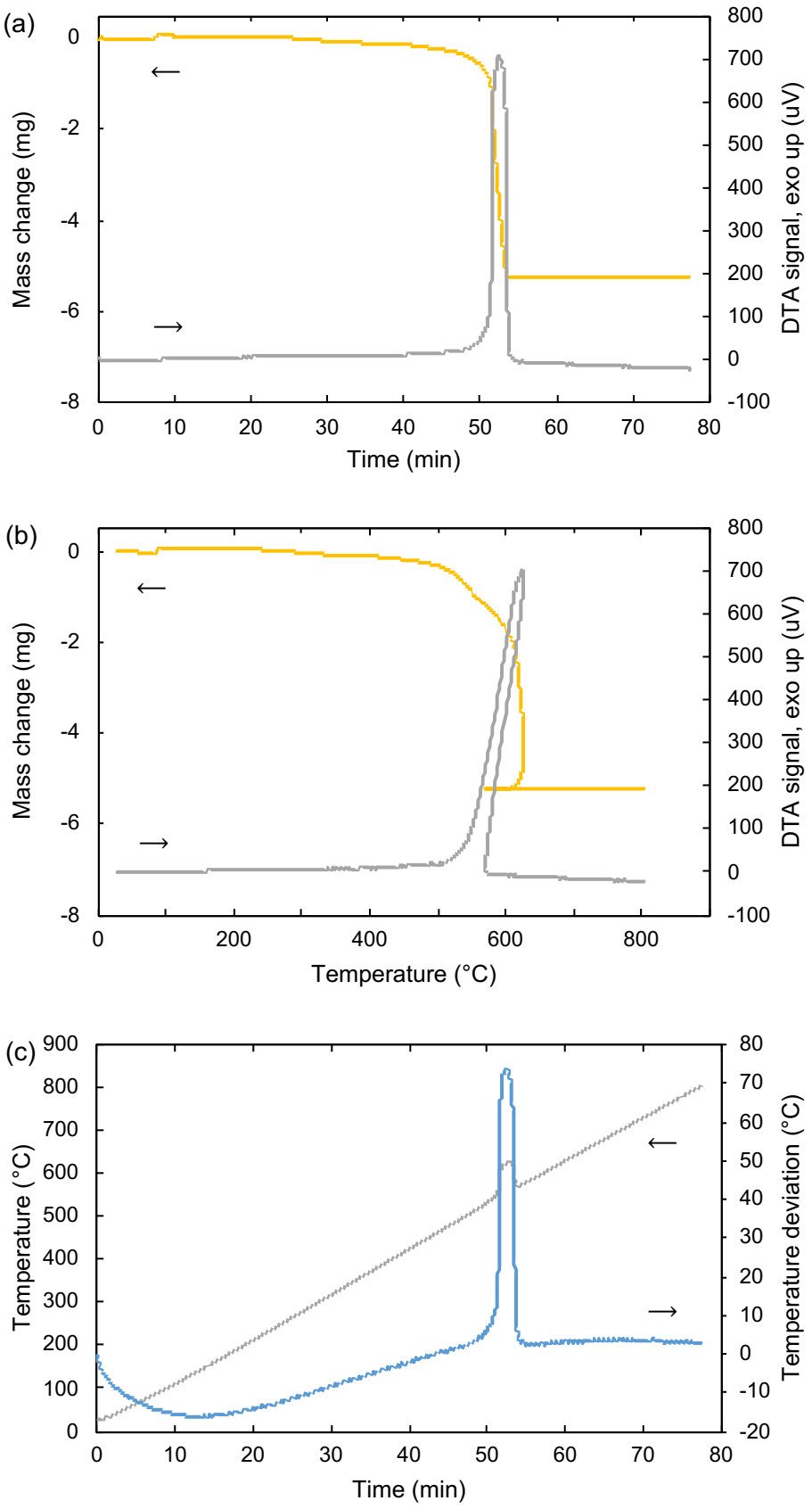

Fig. S16. Thermogravimetry and differential thermal analysis of ZIF-7 nanoparticles post-activation, shown as a function of time (a) and temperature (b). Sample temperature data and deviation from programmed temperature profile are shown in (c).

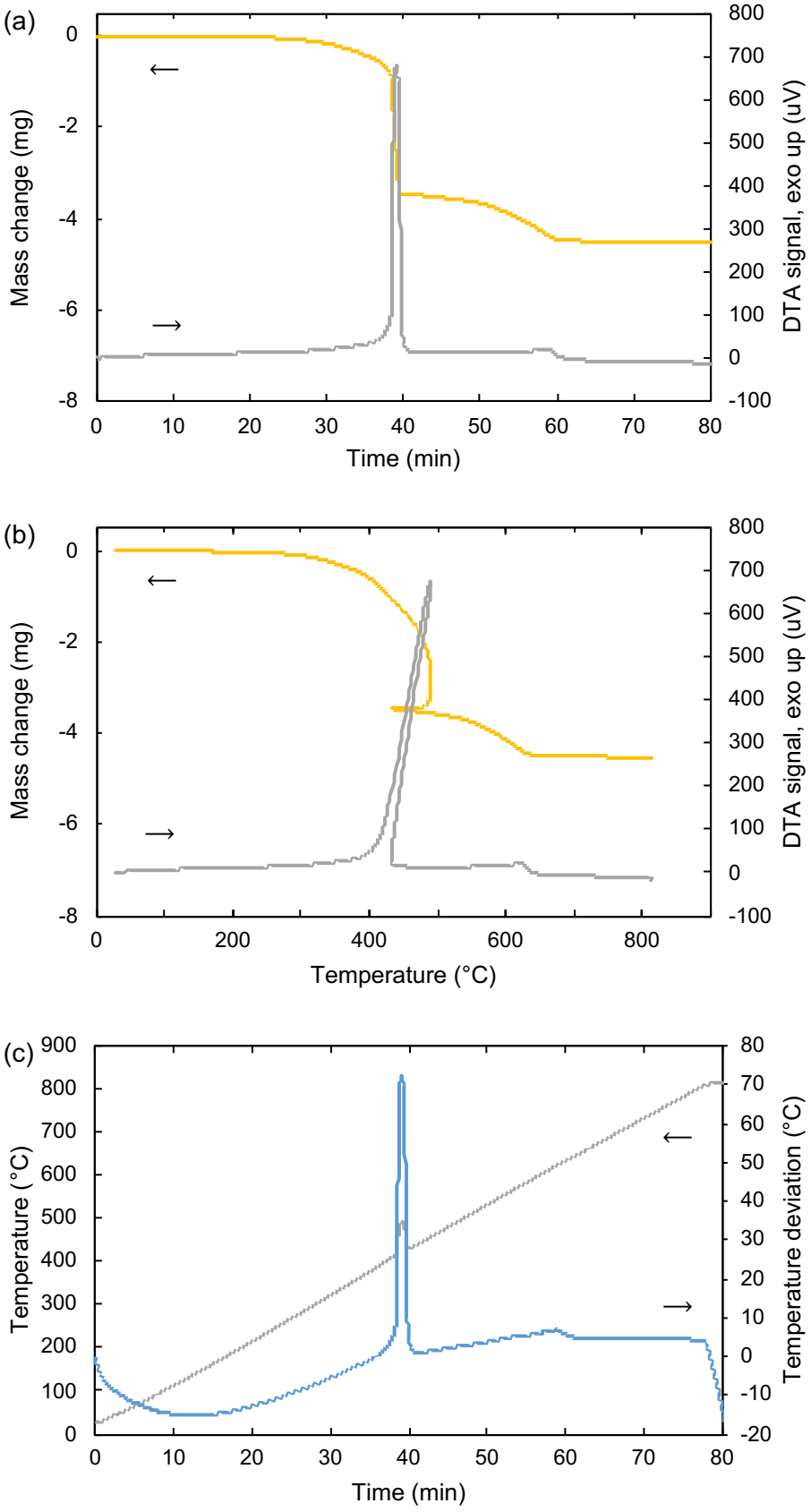

Fig. S17. Thermogravimetry and differential thermal analysis of ZIF-8 nanoparticles post-activation, shown as a function of time (a) and temperature (b). Sample temperature data and deviation from programmed temperature profile are shown in (c).

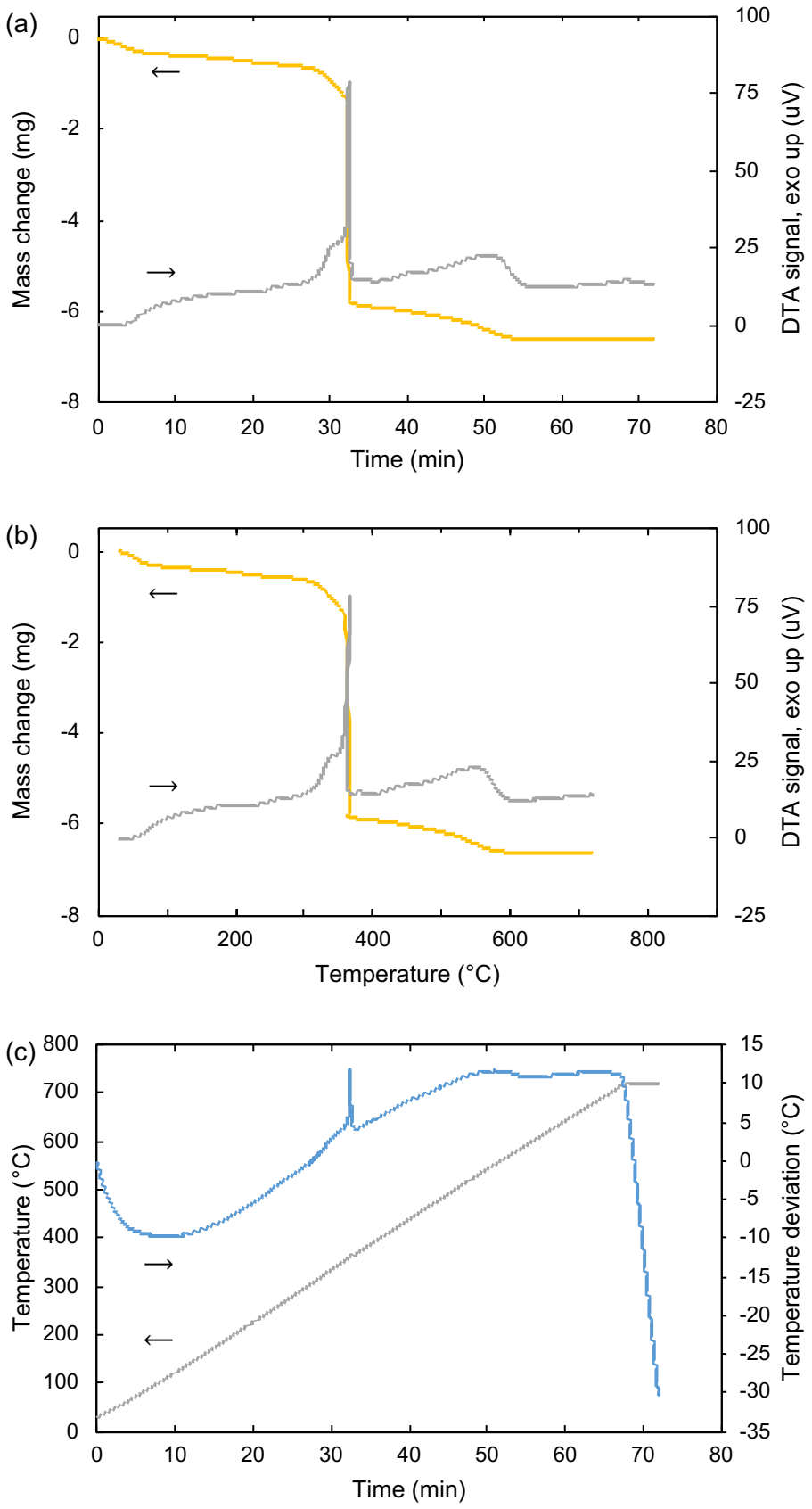

Fig. S18. Thermogravimetry and differential thermal analysis of ZIF-65-Zn nanoparticles post-activation as a function of time (a) and temperature (b). Sample temperature data and deviation from programmed temperature profile are shown in (c).

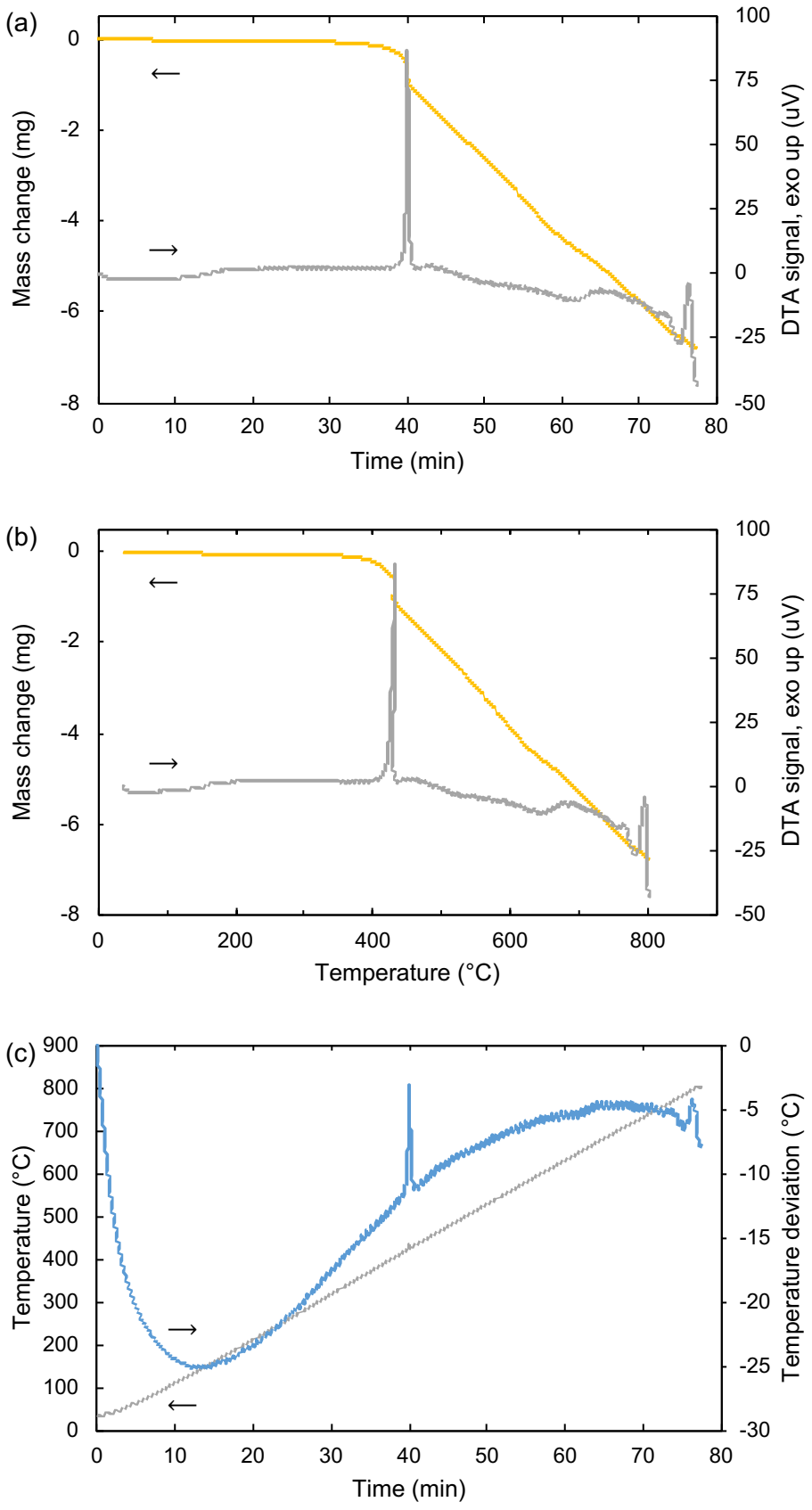

Fig. S19. Thermogravimetry and differential thermal analysis of ZIF-71 nanoparticles post-activation as a function of time (a) and temperature (b). Sample temperature data and deviation from programmed temperature profile are shown in (c).

S8. Sensing experiments: selectivity and VOC discrimination.

Saturated vapour sensing was performed with the following experimental setup. The MSS coated with various ZIFs was mounted on a chamber and the chamber was carefully sealed with an O-ring. Two mass flow controllers (MFCs; FCST1005C-4F2-F100-N2, purchased from Fujikin Inc.) were utilized to introduce nitrogen into the chamber at the flow rate of 100 mL/min. One MFC was for purging (*i.e.* accelerating desorption of adsorbents), and the other one was for introducing sample vapor together with nitrogen as a carrier. In the present case, 1 mL of 26 sample liquids (pure water, formaldehyde solution (35–38%), acetic acid, methanol, ethanol, isopropanol, 1-butanol, 1-pentanol, acetone, methyl ethyl ketone, *n*-hexane, *n*-heptane, *n*-octane, *n*-nonane, *n*-decane, *n*-undecane, *n*-dodecane, benzene, toluene, xylene, 1,2-dichlorobenzene, 1,3-dichlorobenzene, chloroform, ethyl acetate, tetrahydrofuran and *N,N*-dimethylformamide; vapour pressures are given in Table S3) was added into a small vial capped with a rubber lid. Two needles connected to a PTFE tube was stuck into the headspace of the vial through the rubber lid. One end of the PTFE was connected to MFC and the other end of the PTFE tube was connected to a vacant vial, so-called 'mixing vial' to make the mixed gas sample homogeneous. Another PTFE tube stuck into the mixing vial was connected to the chamber. Another MFC and vacant vial were set in the same way and connected to the mixing vial. The two MFCs were switched every 30 seconds to perform a sample introduction-purging cycle. This cycle was repeated four times, and the data were recorded at the bridge voltage of –0.5 V and sampling rate of 20 Hz. The data collection program was designed by LabVIEW (National Instruments Corporation). All the above experiments were conducted under an ambient condition without any temperature/humidity control.

The response of four blank MSS membranes was measured to confirm that the observed responses of the MOF–MSS were due to the MOF receptor layers. As can be seen in Figs. S20 and S21, the outputs of the blank devices change by 0.01–0.02 mV upon introduction of 20% saturated water or methanol vapour, and the drift of the signals over the course of the 270 s experiment is 0.01–0.06 mV. These values are small compared with output signals of 0.5–8 mV from the MOF–MSS.

Table S3. Selected VOCs and their vapour pressures[a] at 298 K.

VOC class	VOC	Vapour pressure (mm Hg)	(ppm)
Alcohols	Methanol	125.79	165507
	Ethanol	65.58	86294
	Isopropanol	51.41	67651
	1-Butanol	6.60	8681
	1-Pentanol	2.34	3081
Carbonyls	Acetone	229.92	302523
	N,N-dimethylformamide[b]	3.47	*4564*
	Acetic acid	8.38	11026
	Methyl ethyl ketone	87.69	115383
	Formaldehyde[c]	52.00	68421
	Ethyl acetate	95.94	126241
Arenes	Benzene	80.48	105897
	Toluene	29.00	38156
	1,2-Dichlorobenzene[b]	1.48	*1951*
	1,3-Dichlorobenzene[b]	2.28	*2994*
	Xylene	6.66	8769
	Hexane	147.70	194341
Alkanes	Heptane	44.85	59019
	Octane	14.80	19480
	Nonane	4.91	6458
	Decane	1.59	2095
	Undecane	0.42	558
	Dodecane	0.15	196
Other	Water[f]	0.03	41.67
	Tetrahydrofuran (THF)	165.26	217452
	Chloroform	191.14	251496

[a] Values calculated from Antoine coefficients obtained from The *Yaws' Handbook of Vapor Pressure*.[7] [b] Estimate; temperature lies outside valid range for coefficients. [c] Based on data at 37 °C from sigmaaldrich.com. [d] Values calculated by NIST based on data from Bridgeman *et al*.[8]

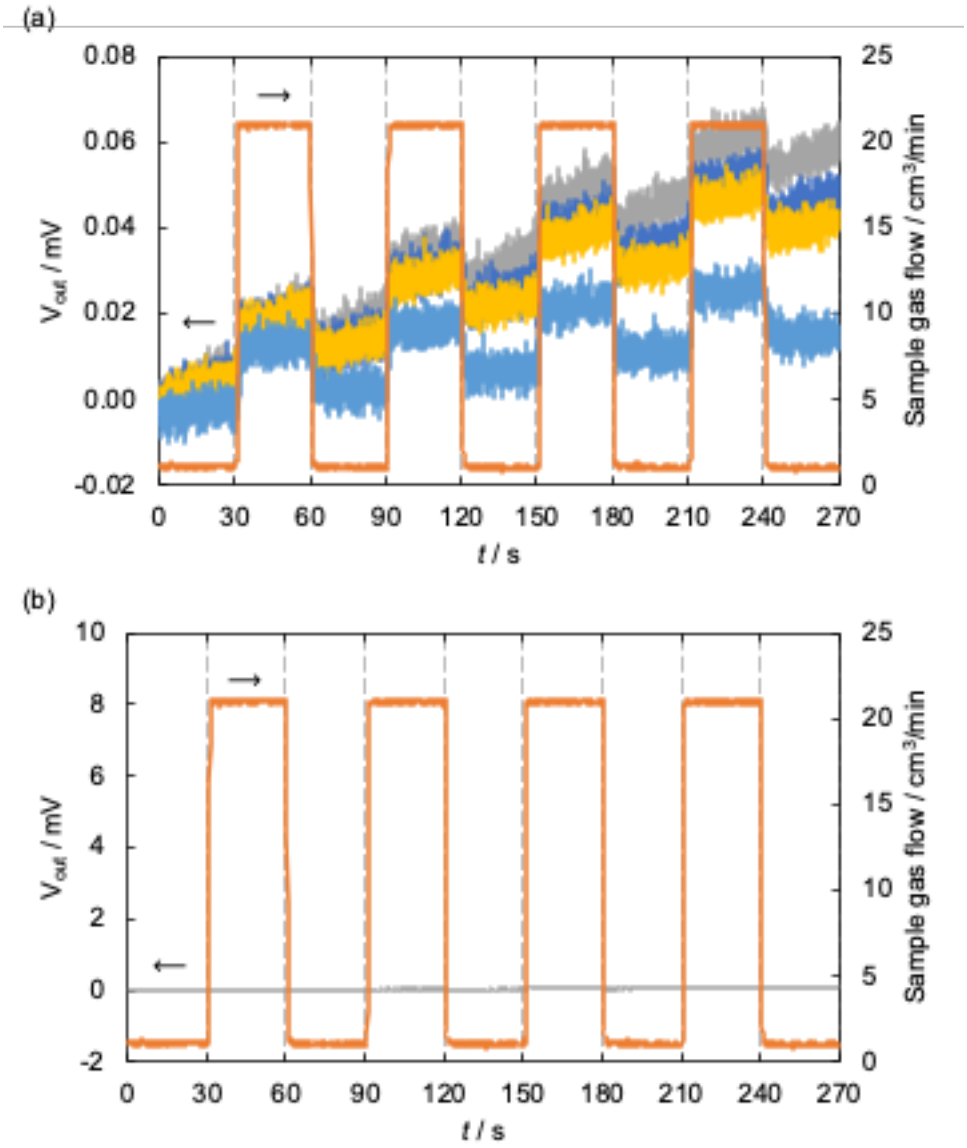

Fig. S20. Response of blank MSS membranes to 20 % saturated water vapour: (a) output voltage as a function of time over four ON-OFF cycles for four different membranes (grey, navy, yellow, light blue), and (b) the response of one blank membrane, scaled to match Fig. 2a in the main manuscript.

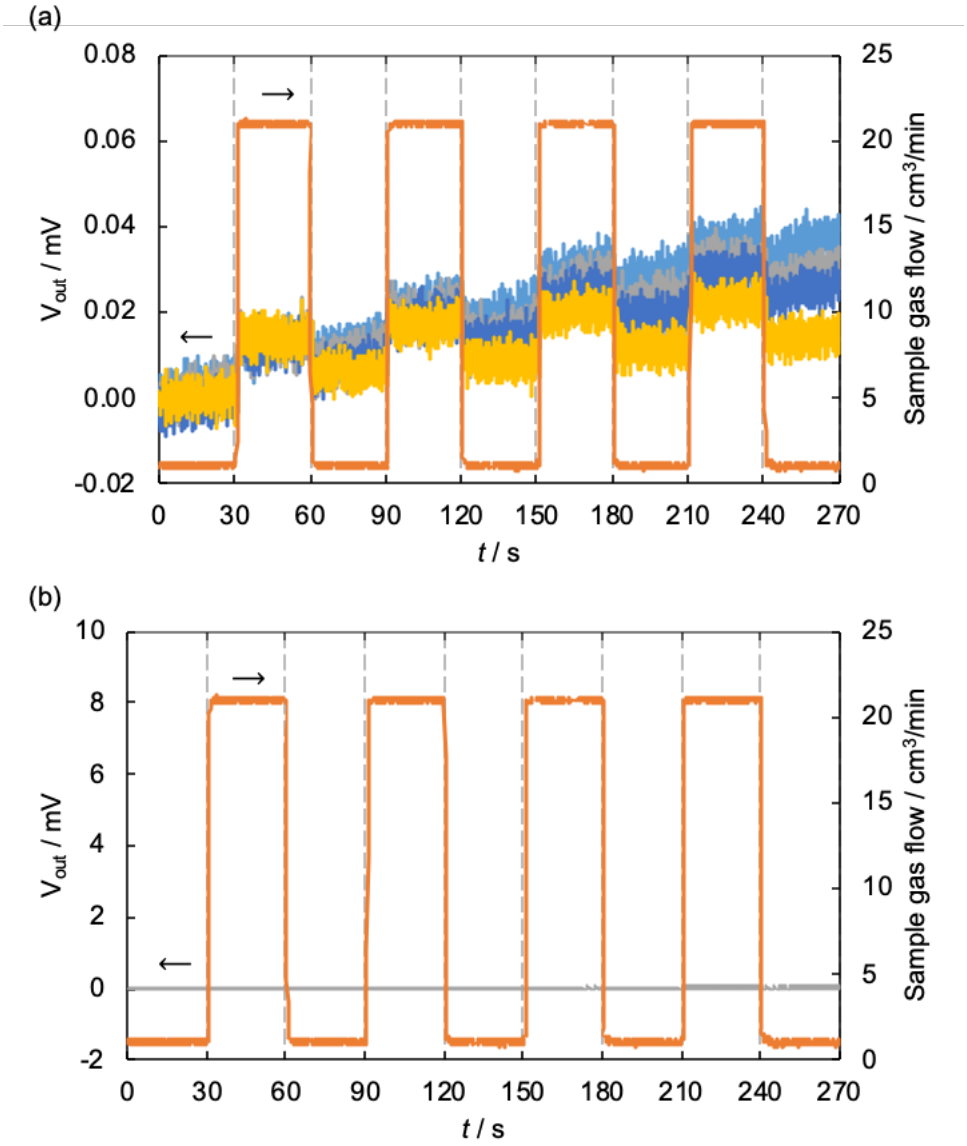

Fig. S21. Response of blank MSS membranes to 20 % saturated methanol vapour: (a) output voltage as a function of time over four ON-OFF cycles for four different membranes (grey, navy, yellow, light blue), and (b) the response of one blank membrane, scaled to match Fig. 2a in the main manuscript.

S9. Sensing experiments: sensitivity and response time.

For sensing experiments in much lower concentration ranges, we designed another measurement system. The MSS chip coated with various ZIFs was mounted in a Teflon chamber, and the chamber was carefully sealed with O-rings. The chamber was placed in a constant temperature bath kept at 25 °C. The sample gases—the vapors of the 12 solvents (pure water, ethanol, 1-hexanol, hexanal, *n*-heptane, methylcyclohexane, toluene, ethyl acetate, acetone, chloroform, aniline and propionic acid) generated via bubbling—were injected into the chamber with a gas flow system equipped with three MFCs. Nitrogen was used as a carrier gas. The concentrations of the sample gases were calibrated by measuring the decrease in the weight of the solvents before and after a gas flow. The relative humidity (RH) was controlled by providing a saturated water vapor to the gas flow line. The concentration of the sample gases and the humidity of the carrier gas were adjusted by controlling the flow rates of the three MFCs. The total gas flow rate of the three MFCs was set at 100 mL/min. The surface stress caused by the gas adsorption/desorption in the ZIF layer was electrically read by a Wheatstone bridge circuit consisting of the piezoresistors embedded on the bridges.[9] In the present study, a voltage of –0.5 V was applied to the circuit, and the relative resistance changes of piezoresistors were detected as output signals. Each measurement was performed through 10 cycles of 10 seconds sample injection and 10 seconds nitrogen purge. The sample gases were diluted to 2, 5 and 10% of their saturated vapor concentration. The carrier gas was humidified at 0%, 10%, 40%, and 70% RH.

S10. Principal component analysis for VOC discrimination

Principal component analysis (PCA) was performed for discrimination of the 26 samples, following the methodology of Shiba *et al.*[10] To perform PCA, features of a signal measured by the MSS were expressed by four parameters which are defined as follows:

$$\text{Parameter 1: } (b - a)/(t_b - t_a) \quad (1)$$
$$\text{Parameter 2: } (c - b)/(t_c - t_b) \quad (2)$$
$$\text{Parameter 3: } (d - c)/(t_d - t_c) \quad (3)$$
$$\text{Parameter 4: } (c - a), \quad (4)$$

where a, b, c, d, e, t_a, t_b, t_c, and t_d are denoted in Fig. S22. In this case, $t_b = t_a + 5$ [s], $t_c = t_a + 30$ [s], and $t_d = t_a + 35$ [s] were used. Three sets of the parameters were extracted from the latter three signals where $t_a = 90$, 150 and 210 out of the four repeated curves in the response signals, since the latter cycles could provide reproducible signals without initial fluctuations such as mixing of sample gases and pre-adsorbed gases. Then, *Origin* software (ver. 2017) was used to perform PCA. PCA finds projection weights for sensor response data that maximize the total response variance in principal components (PCs), where the dimension capturing the greatest variance is given by PC1, and the second greatest variance (subject to being orthogonal to PC1) is given by PC2.

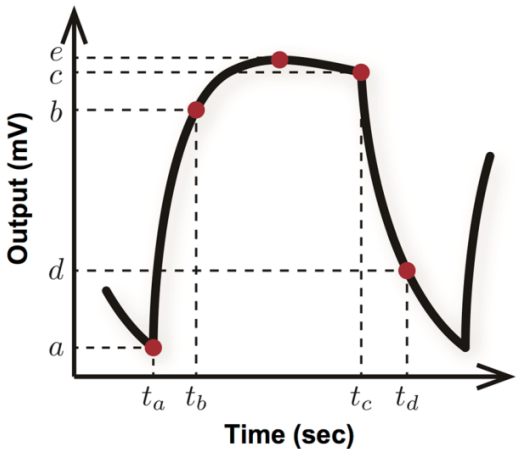

Fig. S22. Schematic of a feature extraction of a signal measured by the MSS. Four parameters are defined as features by using a, b, c, d, e, t_a, t_b, t_c, and t_d. Figure reproduced with permission from Shiba *et al.*[10]

S11. ZIF-8 response to 26 VOCs – detailed plots

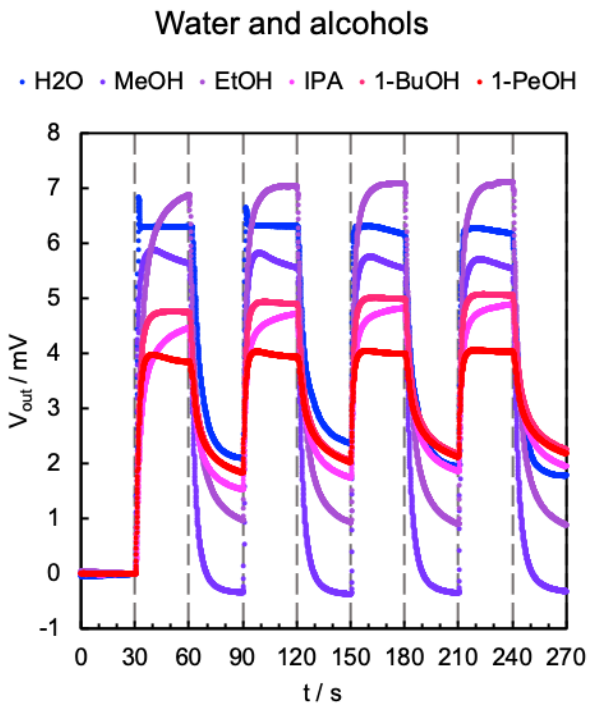

Fig. S23. Response profiles of ZIF-8-MSS fabricated by spray-coating to saturated vapour of water and alcohols.

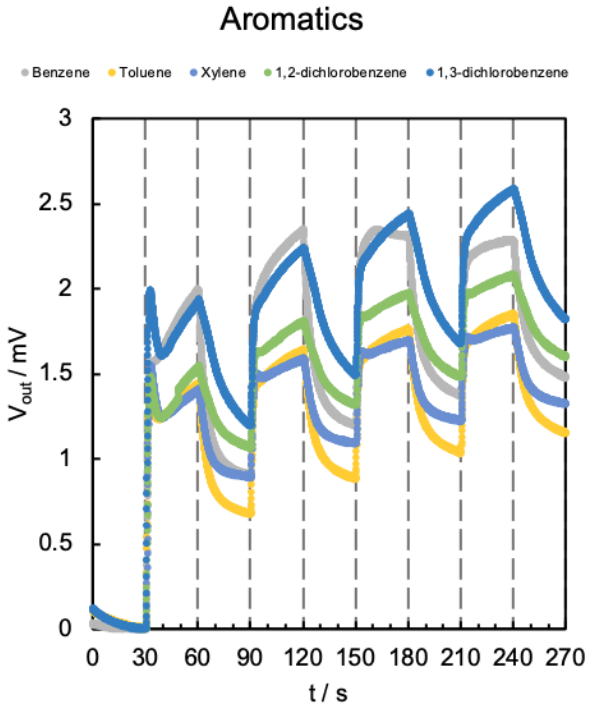

Fig. S24. Response profiles of ZIF-8-MSS fabricated by spray-coating to saturated vapour of aromatic VOCs.

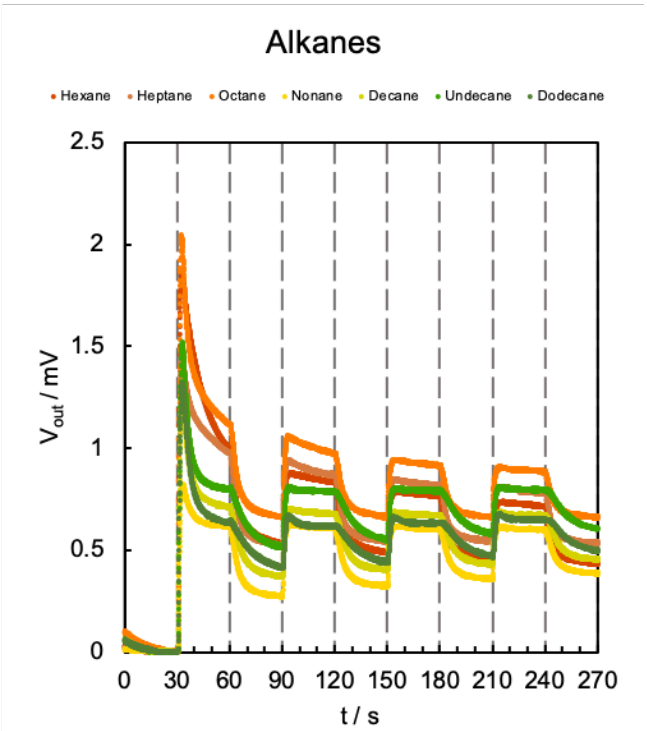

Fig. S25. Response profiles of ZIF-8-MSS fabricated by spray-coating to saturated vapour of linear chain alkanes.

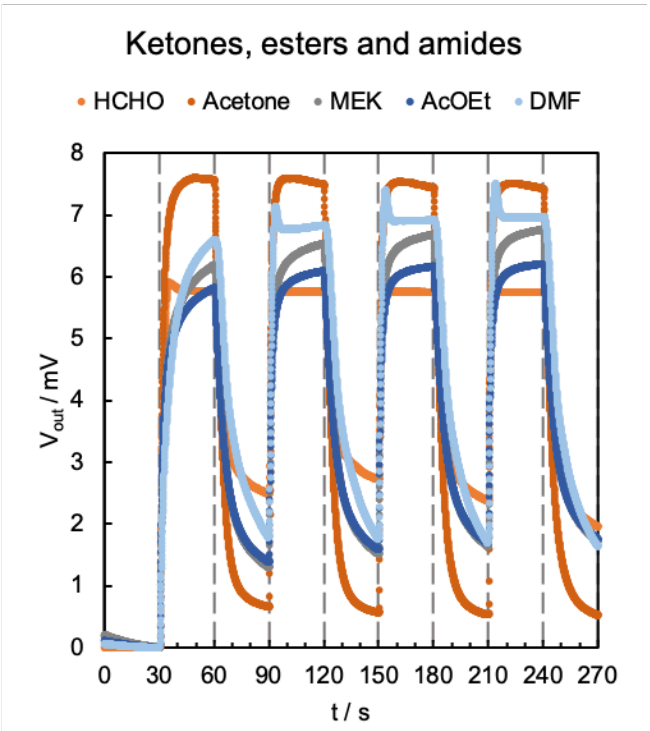

Fig. S26. Response profiles of ZIF-8-MSS fabricated by spray-coating to saturated vapour of ketones, esters and amides. HCHO = formaldehyde (aq.); MEK = methyl ethyl ketone; AcOEt = ethyl acetate; DMF = *N,N*-dimethylformamide.

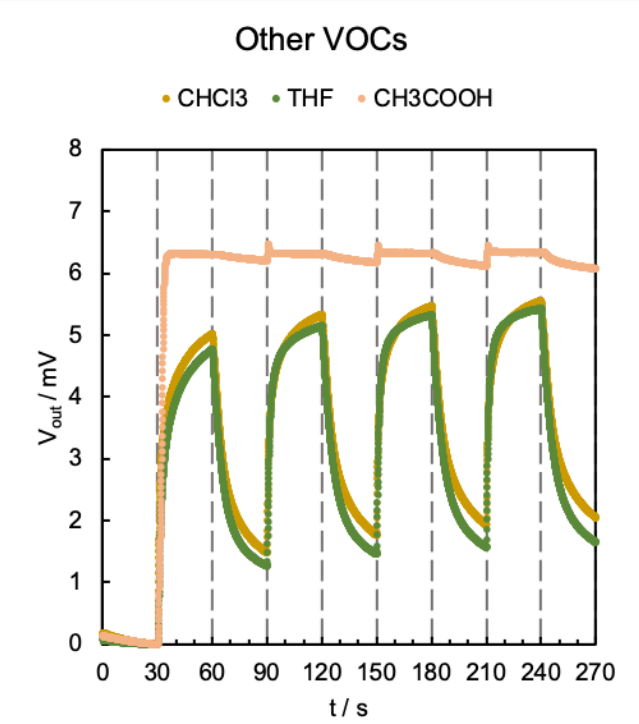

Fig. S27. Response profiles of ZIF-8-MSS fabricated by spray-coating to saturated vapour of other VOCs. CHCl3 = chloroform; THF = tetrahydrofuran; CH3COOH = acetic acid.

S12. Optimisation of receptor layer volume

The receptor layer volume was optimized by measuring the sensor response to selected VOCs as a function of the number of inkjet droplets deposited. The magnitude of responses (Fig. S28) to water, methanol, acetone, heptane and toluene appear to increase linearly with respect to mass up to 900 droplets. Thereafter, maxima are found around 1700–2100 droplets in each case. Response time, defined here as the time taken to reach 80 % of the maximum output voltage, was found to be less than 10 s in most cases without a linear trend with respect to layer volume (Fig. S29). With the exception of the layer of 2500 droplets, both acetone and heptane elicit response times less than 5 s.

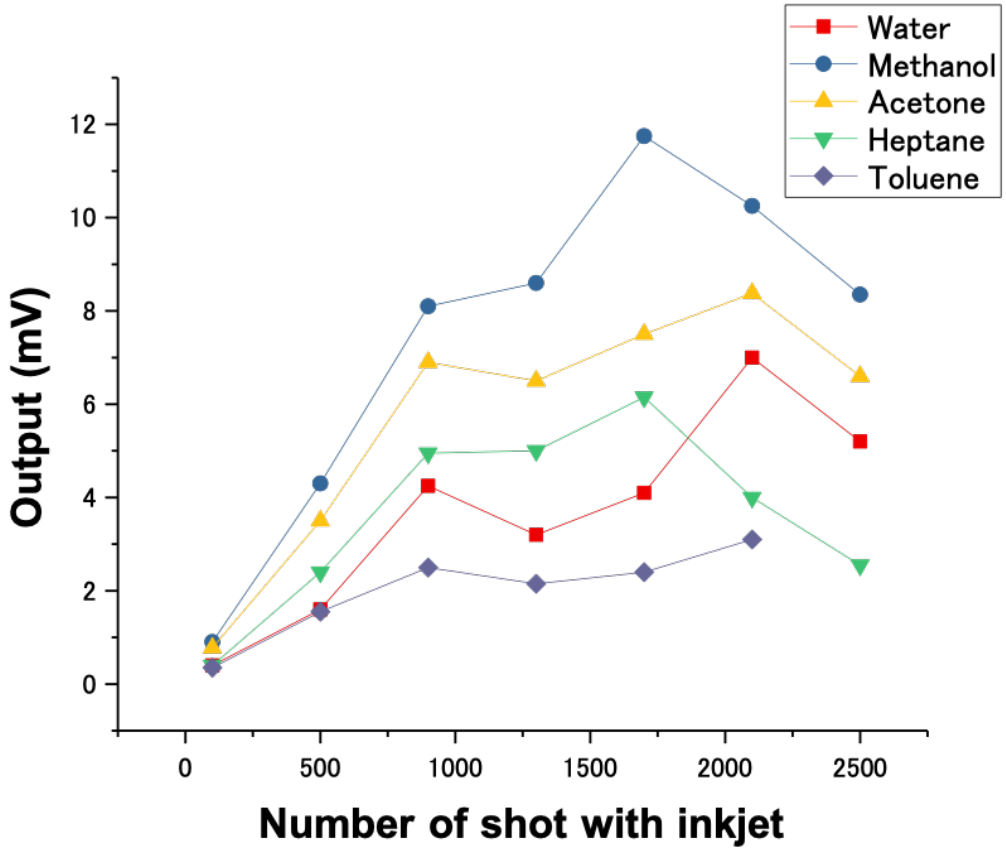

Fig. S28. Output voltage as a function of receptor layer volume, measured as number of inkjet printed droplets, for selected VOCs.

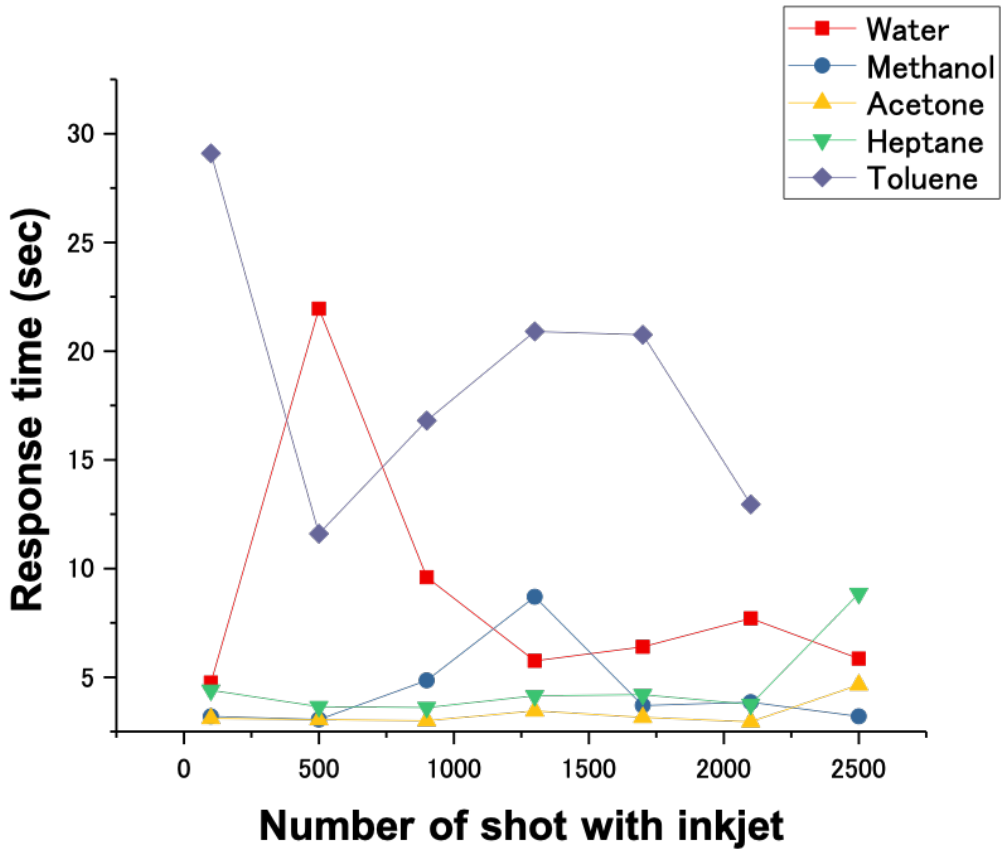

Fig. S29. Output response time (defined here as the time taken to reach 80% of the maximum response) as a function of receptor layer volume, measured as number of inkjet printed droplets, for selected VOCs.

S13. Finite element Analysis

To examine the effects of ZIF-8 receptor layer thickness, t_f, on nanomechanical sensing, we performed numerical calculations through Finite Element Analysis (FEA) using COMSOL Multiphysics® 5.5 with the Structural Mechanics module. The dimensions for the MSS were set as illustrated in Fig. S30. The diameter and thickness of the membrane are 300 μm and 3 μm, respectively. The membrane is suspended by the four sensing beams, in which piezoresistors are embedded (R_1–R_4). The dimensions of each beam in the directions x and y are as follows: sensing beams for R_1 and R_3, 12 μm × 18 μm; sensing beams for R_2 and R_4, 28 μm × 13 μm.

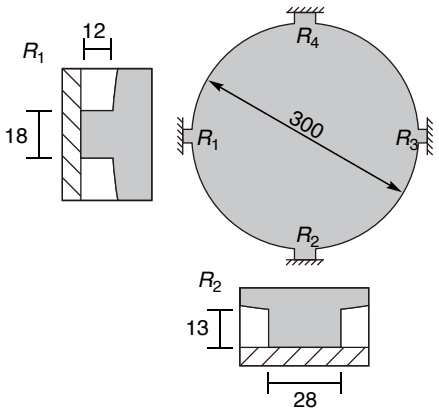

Fig. S30. Configuration of an MSS. The piezoresistor-integrated sensing beams are magnified in the insets. All images are illustrated in top-view. Numbers indicate the dimensions in μm.

A receptor layer with radius, r_f, of 145 μm was placed on the membrane at the center and the thickness of the receptor layer, t_f, was varied from 0.1 μm to 25 μm, its Young's modulus, E_f, was varied with representative values of 2.973 ± 5%, 3.145 ± 5% and 7.06 ± 5% (corresponding to Young's modulus values of ZIF-8 when evacuated, filled with DMF and in monolithic form, respectively[11,12]), and its Poisson's ratio, ν_f, was varied between representative values of 0.3 and 0.45.[13] To the receptor layer, isotropic internal strain, ε_f, ranging from 1×10^{-6} to 3×10^{-4} was applied. These results are shown in Figures S31 and S32.

Each geometry was meshed over 20,000 elements, which give sufficient resolution for the present simulation. In the case of an MSS, the surface stress on the membrane is transduced to the four sensing beams as an amplified uniaxial stress, resulting in the changes in electrical resistance of the piezoresistors embedded in the beams. We calculated the total resistance change, $\Delta R/R|_{\text{total}}$ obtained from the Wheatstone bridge circuit composed of the four piezoresistors, providing the sensing signals of MSS. The p-type piezoresistors of the MSS are fabricated by doping boron onto a single crystal Si with (100) surface to take advantage of its high piezocoefficient.[9,14–17] Assuming in-plane stress (*i.e.*, $\sigma_z = 0$), relative resistance change can be described as:[17,18]

$$\frac{\Delta R_i}{R_i} \approx \frac{1}{2}\pi_{44}\left(\sigma_x - \sigma_y\right), \tag{5}$$

where π_{44} (~138 × 10^{-11} [Pa^{-1}]) is one of the fundamental piezoresistance coefficients of the silicon crystal, and σ_x, σ_y and σ_z are stresses induced on the piezoresistors in [110], [1–10] and [001] directions of the silicon crystal, respectively. The subscript of "*i*" indicates the position of the piezoresistors on the MSS can be seen in Fig. S30 and the previous literature.[9,14] The total resistance change, $\Delta R/R|_{\text{total}}$, of all four piezoresistors can be approximately given by the following equation:

$$\left.\frac{\Delta R}{R}\right|_{\text{total}} = \left(\frac{\Delta R_1}{R_1} - \frac{\Delta R_2}{R_2} + \frac{\Delta R_3}{R_3} - \frac{\Delta R_4}{R_4}\right). \tag{6}$$

Due to the symmetric geometry, Eq. (6) can be reduced to the following equation:

$$\left.\frac{\Delta R}{R}\right|_{\text{total}} = 2\left(\frac{\Delta R_1}{R_1} - \frac{\Delta R_2}{R_2}\right). \tag{7}$$

The signal output (intensity) of the full Wheatstone bridge (V_{out}) is given by:

$$V_{\text{out}} = \frac{V_B}{4}\left.\frac{\Delta R}{R}\right|_{\text{total}}, \tag{8}$$

where V_B is bias voltage applied to the bridge.[9,14] A fixed constraint was applied on the outer edges of the four sensing beams (Fig. S30).

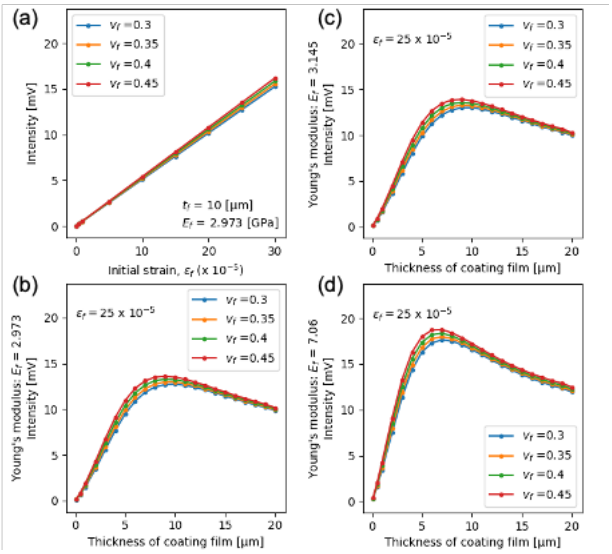

Fig. S31. MSS response as a function of strain (a) and thickness at Young's modulus values of 2.973, 3.145 and 7.06 (b–d, respectively) with Poisson's ratio values from 0.3 to 0.45.

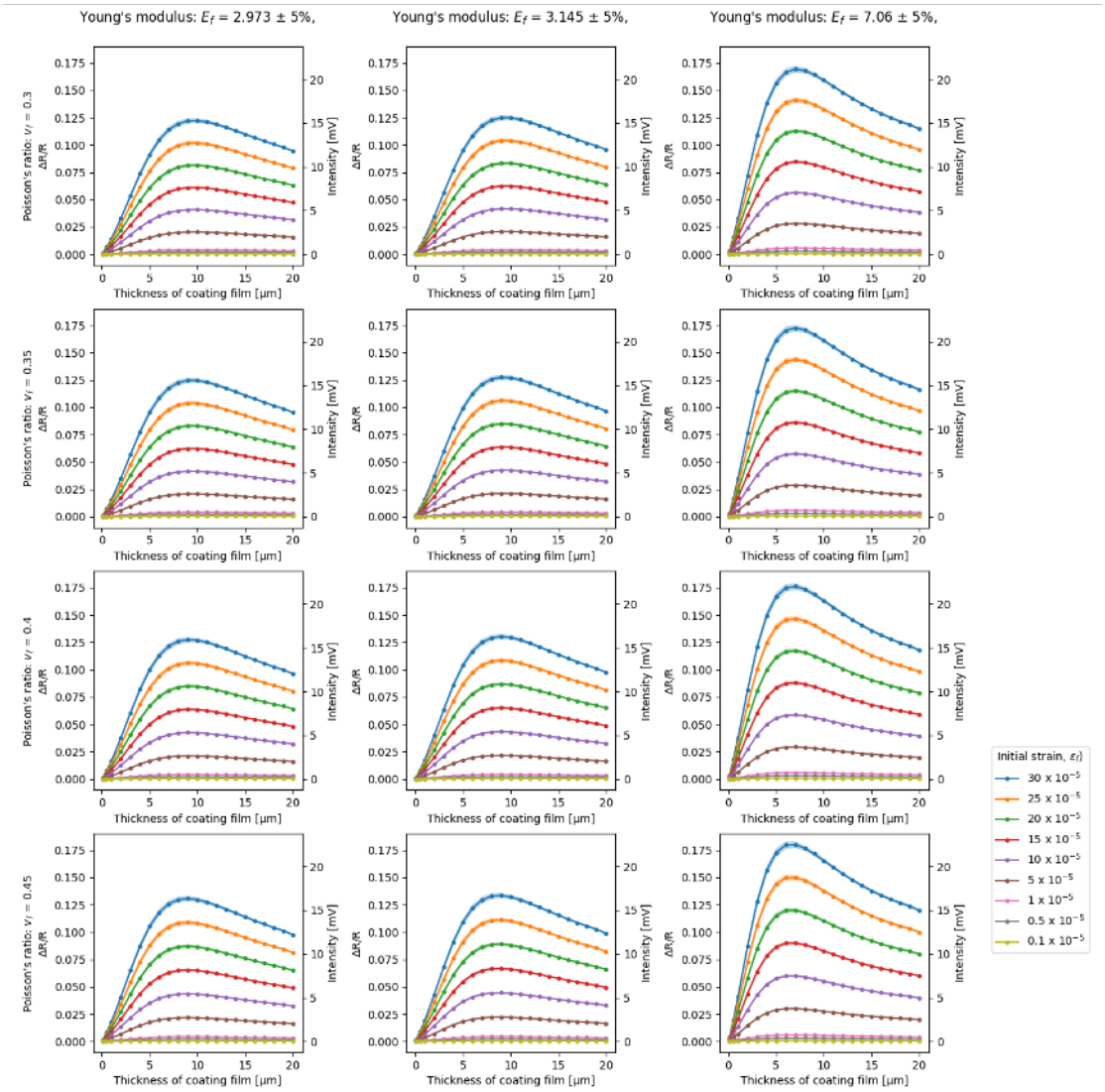

Fig. S32. MSS response as a function of receptor layer thickness, strain, Young's modulus and Poisson's ratio.

S14. Estimated thickness of ZIF-8 on the membrane of MSS

When we coat N droplets of ZIF-8 solution by inkjet spotter, the volume of spotted solution, $V_{\text{sol.}}$ [mL], is given by:

$$V_{\text{sol.}} = V_{\text{drop}} \cdot N, \tag{9}$$

where V_{drop} denotes the volume of one droplet [mL/droplet]. When the concentration of ZIF-8 solution is C [g/mL], the volume of ZIF-8 layer on the membrane of MSS, V_f, is given by:

$$V_f = \frac{V_{\text{drop}} \cdot N \cdot C}{\rho}, \tag{10}$$

where ρ denotes the density of ZIF-8 (solid) [g/mL]. When the ZIF-8 receptor layer forms a cylindrical structure, the thickness of ZIF-8 layer, t_f [cm], is given by:

$$t_f = \frac{V_{\text{drop}} \cdot N \cdot C}{\rho} \Big/ \pi r_f^2, \tag{11}$$

where r_f denotes the radius of cylindrical receptor layer [cm]. The thickness, t_f, of the 2100 shots layer is calculated from the values given in Table S4, using eq. (11) as follows:

$$\begin{aligned} t_f[\text{cm}] &= \frac{0.3 \times 10^{-6} \cdot 2100 \cdot 1.0 \times 10^{-3}}{0.92} \Big/ (\pi \times (1.45 \times 10^{-2})^2) \\ &= 10.4 \times 10^{-4}\ [\text{cm}] \\ &= 10.4\ [\mu\text{m}]. \end{aligned} \tag{12}$$

Table S4. Parameters for ZIF-8 receptor layer thickness calculation.

Descriptions		Default values		
Volume of one droplet	V_{drop}	~ 0.3	[nL / shot]	= ~ 0.3×10^{-6} [cm^3/droplet]
Number of droplets	N	2100	[shot]	
Conc. of ZIF-8	C	1.0	[mg/mL]	= 1.0×10^{-3} [g/cm^3]
Density of ZIF-8	r	0.92	[g/mL]	= 0.92 [g/cm^3]
Radius of receptor	r_f	145	[μm]	= 1.45×10^{-2} [cm]

S15. Relative responses of 2 × 2 array of ZIFs to 26 VOCs

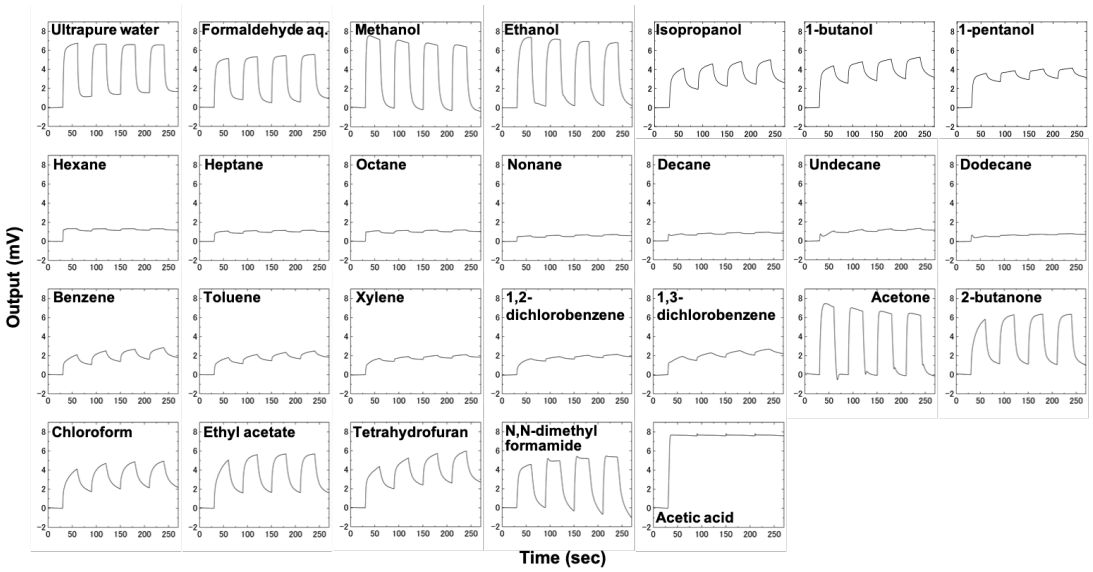

Fig. S33. Response profiles of ZIF-7-MSS membrane to 26 VOCs.

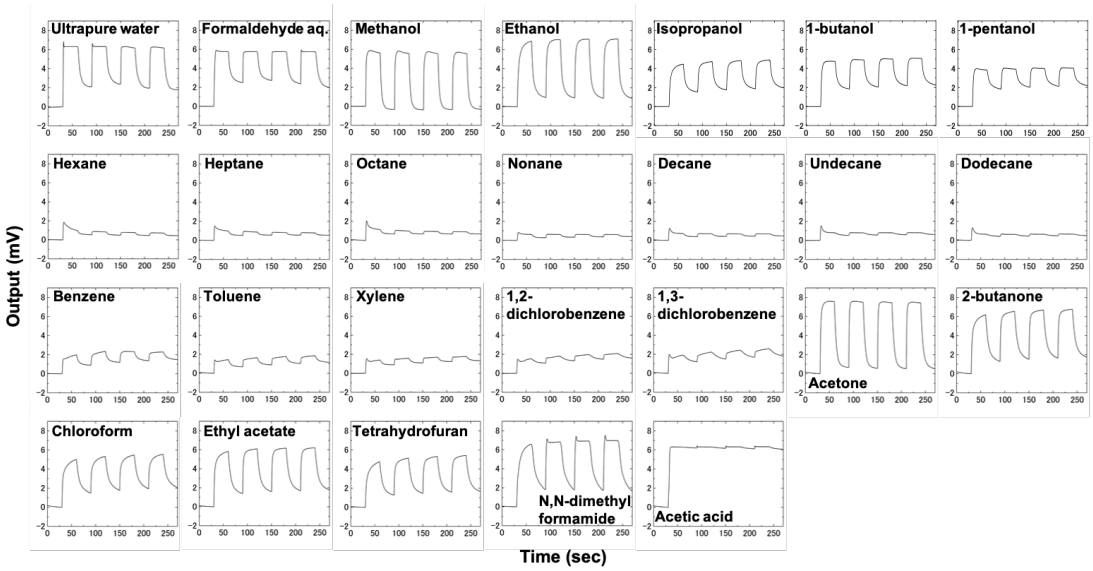

Fig. S34. Response profiles of ZIF-8-MSS membrane to 26 VOCs.

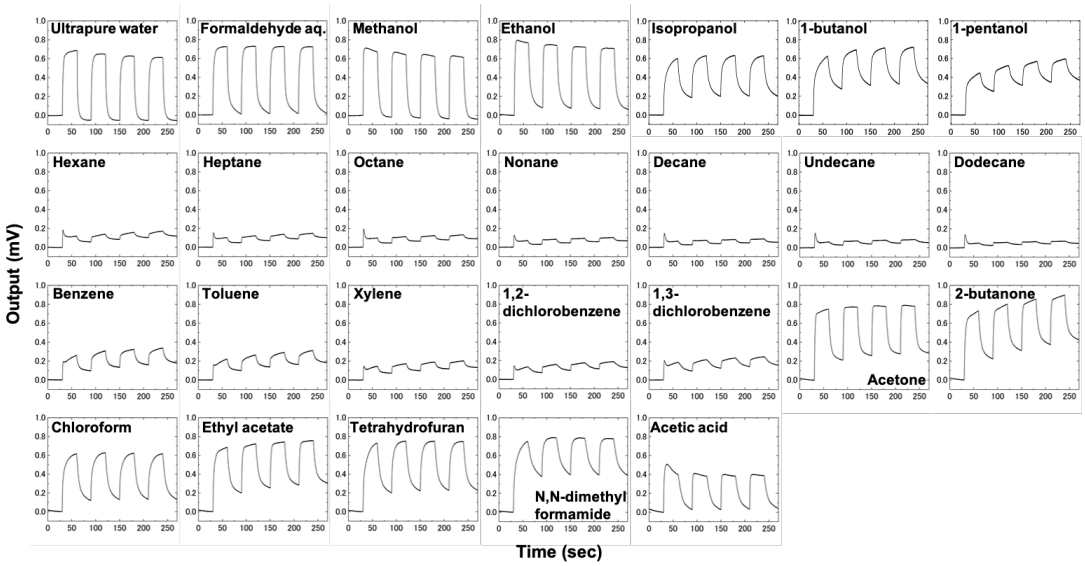

Fig. S35. Response profiles of ZIF-65-Zn-MSS membrane to 26 VOCs.

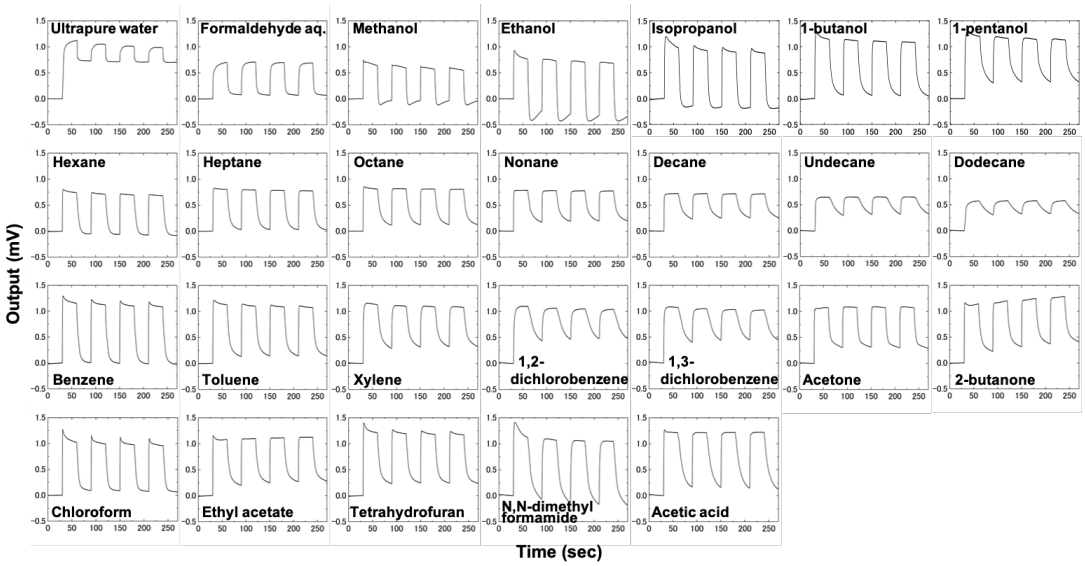

Fig. S36. Response profiles of ZIF-71-MSS membrane to 26 VOCs.

S16. Principal component analysis plots using three PCs.

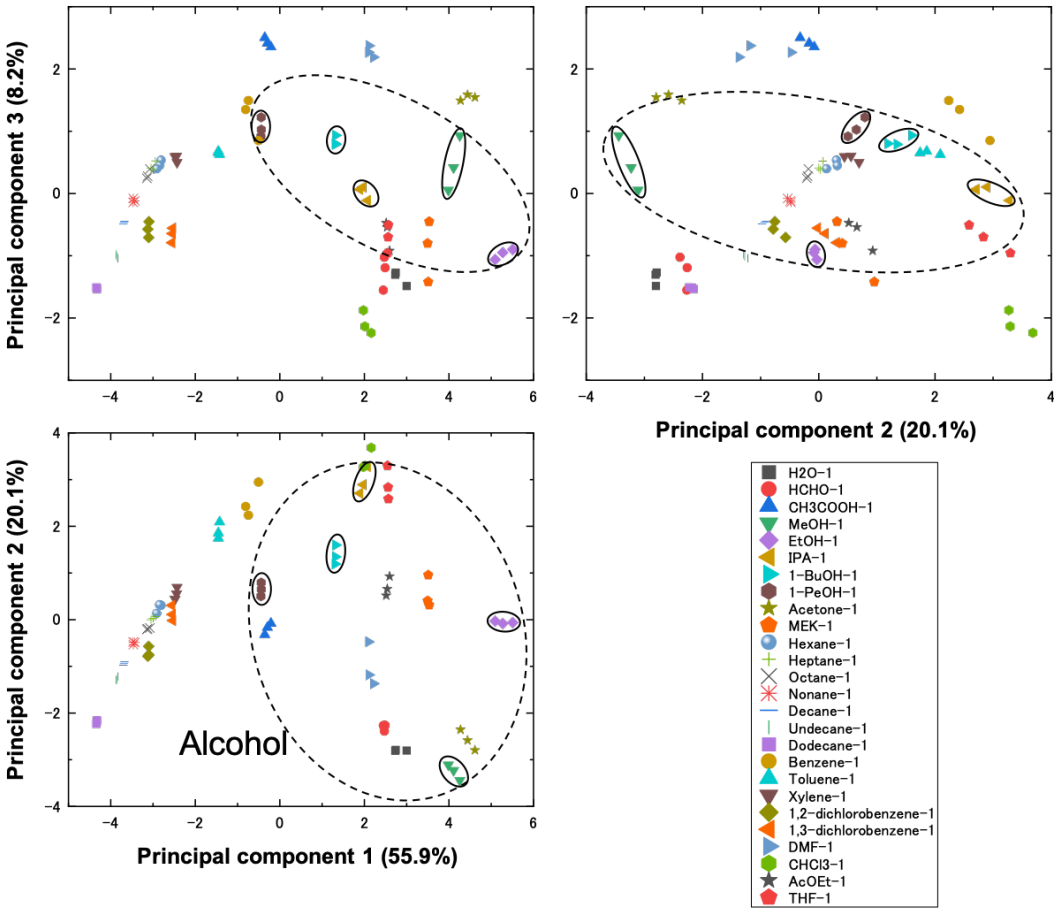

Fig. S37. Principal component analysis, showing combinations of PC1, 2 and 3. Alcohol responses are individually grouped within solid ellipses.

S17. Comparison of selected MOF-based sensors.

Table S5. Comparison of selected MOF-based sensors.

MOF	Fabrication method	Device type	Analytes	Sensitivity / ppm	Response time / s	Ref.
Strain-based						
ZIF-8	Conversion of ZnO nanorods	Microcantilever (frequency change)	Methanol, ethanol, 1-propanol	3-10	10-100	[19]
ZIF-8	Conversion of ZnO nanorods	Microcantilever (deflection)	Methanol, ethanol, 1-propanol	10-20	100-500	[19]
HKUST-1	Growth on self-assembled monolayer	Microcantilever (deflection)	H_2O, methanol, ethanol, CO_2	1000	10	[20]
ZIF-8, 7, 65, 71	Inkjet printing	Membrane-type Surface stress Sensor (MSS)	Various VOCs	0.1-30	1-30	This work
Chemoresistive						
$Cu_3(HITP)_2$	Drop-casting	Interdigitated electrodes	Ammonia	≤ 0.5	Not reported	[21]
Cu, Ni-HITP/HHTP	Drop-casting	Interdigitated electrodes	Various VOCs	20	Not reported	[22]
Photonic						
ZIF-8	Direct growth on substrate	Fabry-Perot interferometer	Propane, ethanol	100	> 120	[23]
ZIF-8	Sequential growth	Multilayer MOF/metal Bragg stack	Ethane, ethylene, propane, propylene, H_2	150	Not reported	[24]
HKUST-1	Step-by-step growth	MOF-Si colloidal crystal thin film	H_2O, Ar, ethanol, ethylene, CO_2, carbon disulfide	0.3-2.6	10-60	[25]
Optical						
HKUST-1	Suspension in PTFE filter	LED fibre optic sensor	Water	0.04	23	[26]

S18. References.

1 Y. S. Li, F. Y. Liang, H. Bux, A. Feldhoff, W. S. Yang and J. Caro, *Angew. Chem. Int. Ed.*, 2010, **49**, 548–551.

2 J. Cravillon, S. Münzer, S.-J. Lohmeier, A. Feldhoff, K. Huber and M. Wiebcke, *Chem. Mater.*, 2009, **21**, 1410–1412.

3 M. Tu, C. Wiktor, C. Rösler and R. A. Fischer, *Chem. Commun.*, 2014, **50**, 13258–13260.

4 P. Zhao, G. I. Lampronti, G. O. Lloyd, E. Suard and S. A. T. Redfern, *J. Mater. Chem. A*, 2014, **2**, 620.

5 K. S. Park, Z. Ni, A. P. Cote, J. Y. Choi, R. Huang, F. J. Uribe-Romo, H. K. Chae, M. O'Keeffe and O. M. Yaghi, *Proc. Natl. Acad. Sci. U. S. A.*, 2006, **103**, 10186–10191.

6 R. Banerjee, A. Phan, B. Wang, C. Knobler, H. Furukawa, M. O'Keeffe and O. M. Yaghi, *Science*, 2008, **319**, 939–943.

7 C. L. Yaws and M. A. Satryo, *Vapor Pressure – Organic Compounds*, Elsevier Inc., 2015.

8 O. C. Bridgeman and E. W. Aldrich, *J. Heat Transfer*, 1964, **86**, 279–286.

9 G. Yoshikawa, T. Akiyama, S. Gautsch, P. Vettiger and H. Rohrer, *Nano Lett.*, 2011, **11**, 1044–1048.

10 K. Shiba, R. Tamura, G. Imamura and G. Yoshikawa, *Sci. Rep.*, 2017, **7**, 3661.

11 J. C. Tan, T. D. Bennett and A. K. Cheetham, *Proc. Natl. Acad. Sci. U. S. A.*, 2010, **107**, 9938–9943.

12 T. Tian, J. Velazquez-Garcia, T. D. Bennett and D. Fairen-Jimenez, *J. Mater. Chem. A*, 2014, **3**, 2999–3005.

13 J. C. Tan, B. Civalleri, C. C. Lin, L. Valenzano, R. Galvelis, P. F. Chen, T. D. Bennett, C. Mellot-Draznieks, C. M. Zicovich-Wilson and A. K. Cheetham, *Phys. Rev. Lett.*, 2012, **108**, 1–6.

14 G. Yoshikawa, T. Akiyama, F. Loizeau, K. Shiba, S. Gautsch, T. Nakayama, P. Vettiger, N. F. de Rooij and M. Aono, *Sensors*, 2012, **12**, 15873–15887.

15 W. G. Pfann and R. N. Thurston, *J. Appl. Phys.*, 1961, **32**, 2008–2019.

16 Y. Kanda, *IEEE Trans. Electron Devices*, 1982, **29**, 64–70.

17 Y. Kanda, *Sens. Actuators A. Phys.*, 1991, **28**, 83–91.

18 P. A. Rasmussen, O. Hansen and A. Boisen, *Appl. Phys. Lett.*, 2005, **86**, 203502.

19 C. Yim, M. Lee, W. Kim, S. Lee, G.-H. Kim, K. T. Kim and S. Jeon, *Chem. Commun.*, 2015, **51**, 6168–6171.

20 M. D. Allendorf, R. J. T. Houk, L. Andruszkiewicz, A. A. Talin, J. Pikarsky, A. Choudhury, K. A. Gall and P. J. Hesketh, *J. Am. Chem. Soc.*, 2008, **130**, 14404–14405.

21 M. G. Campbell, D. Sheberla, S. F. Liu, T. M. Swager and M. Dincă, *Angew. Chem. Int. Ed.*, 2015, **54**, 4349–4352.

22 M. G. Campbell, S. F. Liu, T. M. Swager and M. Dincă, *J. Am. Chem. Soc.*, 2015, **137**, 13780–13783.

23 G. Lu and J. T. Hupp, *J. Am. Chem. Soc.*, 2010, **132**, 7832–7833.

24 G. Lu, O. K. Farha, W. Zhang, F. Huo and J. T. Hupp, *Adv. Mater.*, 2012, **24**, 3970–3974.

25 G. Lu, O. K. Farha, L. E. Kreno, P. M. Schoenecker, K. S. Walton, R. P. Van Duyne and J. T. Hupp, *Adv. Mater.*, 2011, **23**, 4449–52.

26 S. I. Ohira, Y. Miki, T. Matsuzaki, N. Nakamura, Y. Sato, Y. Hirose and K.

Toda, *Anal. Chim. Acta*, 2015, **886**, 188–193.